ACS APPLIED MATERIALS & INTERFACES

www.acsami.org Research Article

Valency-Conserved Doping in Infrared Plasmonic Nanocrystals for Supersonic Shock-Resistant Multi-Level Cell Modulation

Do Yoon Park, Ju Hyeon Kang, Sivaprakash Paramasivam, Gordon Duddy, Jordan A. Hachtel, Jon P. Camden, Ikhyun Kim,* and Shin Hum Cho*

Cite This: https://doi.org/10.1021/acsami.5c13073 Read Online

ACCESS | Metrics & More | Article Recommendations | Supporting Information

ABSTRACT: Indium tin oxide (Sn/In_2O_3) is a degenerately doped semiconductor nanocrystal (NC) that exhibits localized surface plasmon resonance (LSPR) in the short-wavelength infrared electromagnetic spectral range. Alternative to metals, the tunability of LSPR is possible in doped semiconductor NCs by controlling the dopant type, doping level, and opto-electrochemical modulation. In this study, dopant oxidation valency in carrier density and LSPR peaks (Sn(IV): 1.04×10^{20} cm^{-3}, 4826 cm^{-1}, Sn(II): 1.05×10^{20} cm^{-3}, 4854 cm^{-1}) is observed to be conserved using differing dopant precursor Sn oxidation states. The robustness and surface oxidation stability were evaluated after extreme shock environment exposure. A synthesized NC-coated substrate was exposed to multicycle supersonic shockwaves at Mach 1.7, pressure 2 MPa, and temperature 864 K, under 5 cycles. Postshock exposed NCs were fabricated into a silicon-on-glass device and LSPR was electrochemically modulated (2 V to −2 V) to reveal multilevel cell (MLC) states through surface-depleted red-shift LSPR spectra. We observe that the device MLC operation, induced by the surface depletion effect, is more apparent in Sn(II) dopant precursor NCs. This is attributed to the delayed incorporation of free carrier donating Sn(IV) toward the NC surface, where the Sn(II) precursor oxidation state undergoes delayed activation into an n-type aliovalent substitutional dopant Sn(IV) during NC growth.

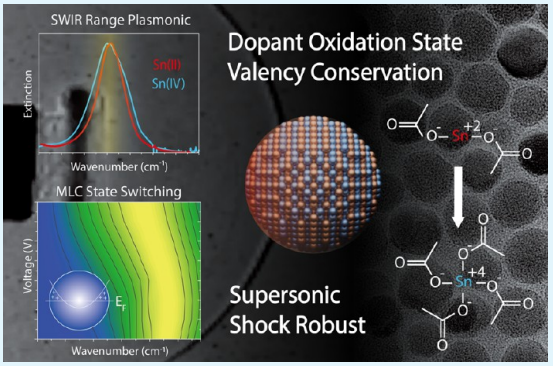

KEYWORDS: *nanocrystal, defect chemistry, plasmon, infrared, semiconductor*

INTRODUCTION

An indium tin oxide (Sn/In_2O_3) nanocrystal (NC) synthesized by colloidal synthesis retains free carriers confined within the NC through degenerate n-type doping.[1] These classes of nanomaterials also have high absorption cross-sectional properties in the short-wavelength infrared (SWIR) 1.4−3.0 μm region. This is due to coherent resonance of low free carrier concentration confined free electrons interacting with incident infrared frequency electromagnetic waves, resulting in an emergent infrared LSPR effect widely observed in these classes of nanoscale materials.[2] These properties are crucially influenced by the dopant oxidation state within the NC lattice as an $Sn_{In}^{\bullet}$ substitutional aliovalent n-type dopant.[3] In prior literature, doped semiconductor plasmonic NCs were synthesized on dopant precursors with an identical oxidation state as the expected substitutional aliovalent n-type dopant valency, especially Sn(IV) acetate, for Sn/In_2O_3 synthesis.[4,5] Two typical acetate-based organometallic compounds exist for Sn, where the Sn(II) acetate oxidation state $[Kr]4d^{10}5s^2$ and Sn(IV) acetate $[Kr]4d^{10}$ electron configuration are most stably preferred.

However, the Sn(IV) dopant is cost inefficient, as Sn(II) acetate has a favorable low industrial price point compared to synthetically biased substitutional aliovalent identical Sn(IV) acetate. Sn(II) acetate is the preferential metal acetate formed from stannous oxide ore and acetic acid reflux reaction.[6] On comparison, Sn(IV) acetate requires additional redox precursor manufacturing steps rooting from metallic Sn^0 to Sn(IV) halide into halide substitution toward Sn(IV) acetate.[7,8] However, according to the Kröger-Vink notation, it is known that Sn^{2+} is not suitable as an n-type substitutional aliovalent dopant ($Sn_{In}^{\bullet}$) for the In^{3+} host lattice metal sites for Sn/In_2O_3 NCs.[9] In this study, when NCs were synthesized using the Sn(II) dopant, the valence of the Sn(II) dopant was converted to Sn(IV) upon NC growth. Thus, retaining the n-type substitution doping mechanism and the existing high-priced Sn(IV) precursor can contribute to a low-cost synthesis supply chain and mass production for SWIR electronic application fields.[6,7,10] However, in addition to the price and

Received: July 4, 2025
Revised: August 12, 2025
Accepted: August 13, 2025

supply chain of indium dopants, indium is a relatively rare and limited element, which could be a significant constraint for long-term commercialization. Although indium tin oxide (ITO, Sn/In_2O_3) exhibits excellent performance in infrared plasmonic applications, the supply issue of indium could be a barrier to large-scale industrialization. Therefore, future research should also focus on developing optimal doping strategies and alternative metal oxide such as aluminum-doped zinc oxide, gallium-doped zinc oxide, and fluorine-doped tin oxide materials to mitigate these resource constraints.[1,7] The aerospace technology domain requires such SWIR applications in attaining light detection and ranging (LIDAR) technological market expansion, along with defense superiority in the aerospace theater.[11] The recent conflicts in Russia and Ukraine have increased the demand for SWIR range infrared sensing, high-speed missile and defense technologies, especially infrared auto guidance technologies such as the Javelin system, a missile tracking infrared sensing system.[12−14] However, these infrared detectors lose their accuracy due to SWIR range sunlight glare, which limits their operation.[15] Therefore, it is possible to protect the accuracy of far-infrared thermal detectors by blocking sunlight in the infrared with a modulable optical filter protecting the detector.[16] Such aerospace LIDAR technologies can be easily spun-off to future mobility vehicles requiring automated driving SWIR range sensing components.[17−19]

Optoelectronic materials with robustness under hypersonic and supersonic environments exposed to strong pressure and high temperature extreme aerospace conditions are in demand for aerospace and defense.[20] The Falcon 9, developed and operated by SpaceX, is a reusable rocket that has successfully launched 403 times as of 2024.[21] One critical component of such a reusable rocket is the surface oxidation robustness of the ballistic vehicle surface such as the payload fairing.[22] Inorganic materials with enhanced surface oxidation robustness include metal oxides such as silicon oxide (SiO_2), titanium oxide (TiO_2), and indium tin oxide (Sn/In_2O_3) typically used in the aerospace industry.[23] Sn/In_2O_3 is known to have excellent optical, electrical, oxidation resistance, electrostatic discharge, and properties, making it suitable as a thin-film material for supersonic speed range aerospace vehicles.[24−26] It is used to protect aircrafts from St. Elmo's Fire by electrostatically dissipating glass surfaces from impacting air molecule friction.[27] Additionally, it has excellent conductive and oxidation resistance materials property, which can be applied to active deicing conductive transparent electrode window surfaces for jet aircrafts.[28] To establish their viability for aerospace and defense applications, optoelectronic coatings must demonstrate robust operational stability under extreme mechanical and thermal conditions. These environments, such as those encountered during high-speed flight operations, are characterized by rapid pressure fluctuations, high strain rates, and intense thermal loads, which can induce surface oxidation and structural degradation.[20,27] Therefore, to simulate these demanding conditions, we subjected the Sn/In_2O_3 NC film to repeated supersonic shockwave exposures (Mach 1.7, 2 MPa, 864 K) prior to device fabrication. This study aims to rigorously evaluate the structural integrity, surface oxidation resistance, and resulting plasmonic performance of the NC film under such duress. The findings are intended to provide a critical assessment of their suitability for advanced supersonic and aerospace systems.

Such optoelectronic and material properties that make Sn/In_2O_3 and inorganic oxides effective in aerospace are attractive in integrating high-performance next-generation semiconductor packaging technologies. Semiconductor corporation players such as TSMC, Intel, and Samsung are ramping up silicon-on-glass (SOG) substrate technologies in competition.[29] The rapid growth of the higher density semiconductor market is driving the need for higher performance compared to traditional semiconductors. In the memory sector, demand for high bandwidth memory has increased, but the current silicon and laminated polymer-based 2.5D packaging Chip-on-Wafer-on-Substrate (CoWoS) technology is limited by heat and power consumption issues, limited by conventional chip packaging substrates.[30] This has led to a significant shift toward alternative substrate materials, where the thermal and mechanical properties of glass are being leveraged to overcome existing packaging limitations. TSMC is reportedly working on glass chip substrates as an alternative to CoWoS packaging technology with Nvidia, and Intel has begun mass production with the goal of commercializing glass substrate-based SOG technology.[31] These state-of-the-art glass substrates are thinner and harder than conventional silicon or organic substrates, and their high thermal resistance reduces warpage and enables up to 10 times more electrical signal transmission in the same area due to low dielectrics insulation.[32] The surface is less prone to thermal expansion warpage where higher density ultrafine line width circuits can be drawn on it, increasing the efficiency of data processing speed and data storage and reducing power consumption.[33]

With the added advantages in integrating glass substrates, we integrate Sn/In_2O_3 NCs into plasmonic memory state modulable multilevel cells (MLC). Surface depletion effect can be deployed to modulate the free carrier concentration confined within the Sn/In_2O_3 NCs.[34] Plasmonic states can be postsynthetically modulated electronically by red-shifting the LSPR resonance frequency, depleting the surface free electron carriers, and modulating the total free carrier concentration within the confined plasmonic NCs. When Sn/In_2O_3 NCs are synthesized by substituting conventional Sn(IV) with exploratory Sn(II) oxidation valency precursors, optoelectrical properties and oxidation states of the known Sn(IV) and Sn(II) valency precursor synthesized NCs are compared pre- and postshock direct exposure conditions at Mach 1.7 observe the robustness to extreme aerospace environments. Surface stability characteristics and the possibilities for plasmonic MLC memory devices operating on glass substrates are explored in this study, expanding plasmonic based electronic architecture components.[35]

EXPERIMENTAL METHOD

Materials. Indium(III) acetate ($In(ac)_3$, 99.99%), tin(IV) acetate ($Sn(ac)_4$), tin(II) acetate ($Sn(ac)_2$), oleic acid (90% technical grade), oleyl alcohol (85% technical grade), tetrachloroethylene (TCE) (anhydrous, ≥99%), and tetramethylammonium bis-(trifluoromethanesulfonyl) imide (97% technical grade) were purchased from Sigma-Aldrich. Surlyn film (Meltonix, Film thickness 60 μm) Plastisol T was purchased from Solaronix. ITO glass (size 20 × 20 × 0.7 mm, sheet resistance 10 Ω/sq) was purchased from Omniscience.

NC Synthesis Using Sn(IV) as a Dopant. Precursor injection with a dopant precursor at Sn 5% at. was prepared by adding oleic acid (10 mL, 31.68 mmol), indium(III) acetate (1386.75 mg, 4.75 mmol), and tin(IV) acetate (88.72 mg, 0.25 mmol) into a 100 mL three-neck round-bottom flask. The mixture was stirred at 600 rpm using a magnetic stir bar and degassed under vacuum at 120 °C for 30 min. Once the degassing was complete, the atmosphere was switched

https://doi.org/10.1021/acsami.5c13073
ACS Appl. Mater. Interfaces XXXX, XXX, XXX−XXX

to nitrogen (N_2). The prepared mixture was transferred to a 50 mL glass syringe. The injection was continuously injected at a controlled rate of 0.2 mL/min into a separate 100 mL 3-neck round-bottom flask containing oleyl alcohol (13 mL, 15.92 mmol) maintained at 290 °C under an N_2 flow to flush out excess water byproduct vapor, initiating the NC growth synthesis reaction. Gradual solution color change to dark blue will be observed due to NC formation and growth.

NC Synthesis Using Sn(II) as a Dopant. In experiments where tin(II) acetate was substituted for study with dopant precursor at Sn 5% at., tin(II) acetate (59.2 mg, 0.25 mmol) replaced tin(IV) acetate, while oleic acid (10 mL, 31.68 mmol) and indium(III) acetate (1386.75 mg, 4.75 mmol) remained constant. The procedure was identical: the mixture was stirred at 600 rpm under vacuum at 120 °C for 30 min to degas the mixture, followed by switching to a nitrogen atmosphere. The degassed mixture was then added at a rate of 0.2 mL/min to a separate 100 mL three-neck round-bottom flask containing oleyl alcohol (13 mL, 41.11 mmol) maintained at 290 °C, completing the synthesis process.

NC Purification. NCs are dispersed in a solvent mixed with a hexane solvent and an isopropyl alcohol (IPA) antisolvent at a 1:1 ratio and centrifuged at 3600 rpm for 3 min. After centrifugation, the solution supernatant is removed, and the remaining solid pellet material is again dispersed in a hexane solvent through vortex mixing. An IPA antisolvent is added to precipitate the NCs, at a hexane to IPA volume 1:1 ratio, and centrifugation is carried out as before. The NC purification is done 3 times. After 3 cycles of centrifugation, the NC pellet is dispersed into 15 mL of hexane. The NC dispersed in hexane without antisolvent is centrifuged at 2000 rpm for 3 min to remove any remaining undispersed aggregates. The supernatant liquid with dispersed NCs was collected as the NC solution sample. All NC solution samples were adjusted to a concentration of 40 mg/mL in hexane for characterization and fabrication.

Fourier Transform Infrared Spectroscopy. Sn/In_2O_3 NCs dispersed in hexane were dried at room temperature to evaporate the hexane solvent and redispersed in TCE. Fourier transform infrared (FTIR) characterization was backgrounded to TCE and analysis was conducted in transmission mode FTIR (Nicolet Summit FTIR) for liquid dispersion measurement. Furthermore, a Widy SenS 320 V-ST InGaAs SWIR camera at a 900 to 1700 nm detection range was used to distinguish infrared visual opacity between Sn/In_2O_3 NCs in hexane.

X-ray Photoelectron Spectroscopy. Samples were prepared by drop casting 50 μL of a solution prepared with Sn/In_2O_3 (tin(IV), tin(II)) NCs on a 1 × 1 cm silicon substrate. Measurements were made at the Korea Basic Science Institute Busan Center (Busan, South Korea) using the Thermo Fisher Scientific Al Kα line (1486.6 eV) as an excitation source. Spectral measurements were performed in an analysis chamber maintained at approximately 10−9 Torr and data analysis was performed using CasaXPS software. Analysis was calibrated on the binding energy (BE) of C 1s peak (BE for C−C = 284.58 eV).

Film Preparation. Sn/In_2O_3 NCs were deposited on ITO glass to obtain the electrochemical spectroscopic properties of NCs. Using the spin coating method, 100 μL of the dispersed NC solution in hexane (40 mg/mL) was spun for 2 min at 1500 rpm. The method was repeated a total of 2 times for a thicker NC coating. Then the film was annealed at 120 °C for 20 min to dry the solvent completely.

SOG Device Fabrication. In the device, the operating electrode consisted of Sn/In_2O_3 NC-coated ITO glass. For the postshockwave-exposed devices, Sn/In_2O_3 NC-coated ITO glass was first exposed to 5 cycles of Mach 1.7 shockwave prior to device fabrication. The counter electrode (CE) was coated with Pt nanoclusters on ITO Glass. Pt nanoclusters were produced by spin-coating 100 μL of Platisol (Solaronix) at 1500 rpm for 2 min. It was then heated under air at 350 °C for 20 min. The thermoformed Surlyn film used to bond the two electrode substrates was fabricated. A 1.0 cm diameter hole was created at the center of the Surlyn film as an optical window, using identical diameter circular hole puncher. A capillary opening passage was cut for injecting the electrolyte into the device. Coated surfaces of the two electrodes were made to face each other and the prepared Surlyn film was placed between layers and fused together by thermoforming onto a hot plate and mechanically pressed together. The glass voids of the Surlyn film were then filled with the electrolyte TMATFSI (1.0 M tetramethylammonium bis-(trifluoromethanesulfonyl) imide in tetraglyme). After electrolyte loading, the device's capillary opening was closed with epoxy resin to seal the electrolyte capillary opening.

In Situ FTIR Electrochemical LSPR Spectra Measurement. The device was measured by using an SP-200 Biologic Potentiostat and Nicolet Summit FTIR Spectrometer (iD1 Transmission Module). After the fabricated device wire input was connected to the potentiostat, the device was loaded to the FTIR transmittance holder with the device optical window aligned to the FTIR transmittance optical aperture. To eliminate spectrometer source beam reflectance off the glass substrate and saturate the detector, the device holder angle was adjusted to 20°. In situ FTIR spectral measurement was performed by cycling the voltage from 2.0 to −2.0 V at 0.5 V intervals and applying a constant potential for 90 s at each interval.

Supersonic Shock Exposure Experiment. A 50 μL portion of the prepared Sn/In_2O_3 NC solution in hexane (40 mg/mL) was dropped on to an ITO glass substrate and spin coated (1500 rpm, 2 min). Two samples of each Sn precursor valency study were prepared through the previous spin coating film preparation method. One of each dopant valency (Sn(IV), Sn(II)) NC was exposed to supersonic shock to prepare four types of samples. The semiautomatic Reddy shock tube applies various acoustic shock pulses to the samples. In this case, the Mach number of each shock pulse is 1.7, with a transient pressure of 2 MPa and a transient temperature of approximately 864 K. High-speed Schlieren imaging was conducted simultaneously to image the Mach disk and shockwave impacting the substrate sample.

Scanning Electron Microscope Imaging. Samples of ITO glass coated with Sn/In_2O_3 NC (Sn(IV), Sn(II)) exposed to five supersonic impact cycles at Mach 1.7 were measured. Cross section imaging was done to confirm the coating status of the sample. The measurement was performed with an electron gun of Schottky field emission type (ZrO/W) imaged at 3.0 kV acceleration voltage, ×100k magnification.

Transmission Electron Microscopy. Transmission electron microscopy (TEM) analysis was performed to confirm the NC shape and size. The sample was dispersed and diluted in hexane, dropped onto a copper TEM grid, and dried under air. The imaging was performed at a 200 kV acceleration voltage. The size distribution of the NCs was evaluated with in ImageJ.

MAC-STEM-EELS (Monochromated Aberration-Corrected, Scanning Transmission Electron Microscopy-Electron Energy Loss Spectroscopy). The NC sample was diluted in 0.1 mg/mL hexane, dropped onto a silicon nitride (SiN) TEM grid (Ted Pella, with 9 each 0.1 mm × 0.1 mm window) with a 15 nm-thickness SiN membrane, and dried under air. A monochromated Nion Ultra-STEM100 was operated at 60 kV by using a probe current of 40 pA (after monochromation) at a nominal 30 mrad semiconvergence angle. The energy resolution of a cold field emission gun electron source is about 300 meV, defined by the full width at half-maximum (fwhm) of the zero loss peak (ZLP). The source was further monochromated by a Nion monochromator, which allows us to reduce the fwhm of the ZLP down to near 15 meV to reach the IR range.

NC Synthesis Using Sn(II) as a Dopant Scale-Up. Precursor injection with a dopant precursor at Sn 5% at. was prepared by adding oleic acid (800 mL, 2534.80 mmol), indium(III) acetate (110,940 mg, 4.75 mmol), and tin(II) acetate (7010 mg, 0.25 mmol) into a 1000 mL three-neck round-bottom flask. The mixture was stirred at 600 rpm using a magnetic stir bar and degassed under vacuum at 120 °C for 60 min. Once the degassing was complete, the atmosphere was switched to nitrogen (N_2). The prepared mixture was transferred to a 300 mL glass syringe. The injection was continuously injected at a controlled rate of 16 mL/min into a separate 1000 mL 3-neck round-bottom flask containing oleyl alcohol (1040 mL, 3288.68 mmol) maintained at 290 °C under an N_2 flow to flush out excess water byproduct vapor, initiating the NC growth synthesis reaction. Gradual

https://doi.org/10.1021/acsami.5c13073
ACS Appl. Mater. Interfaces XXXX, XXX, XXX−XXX

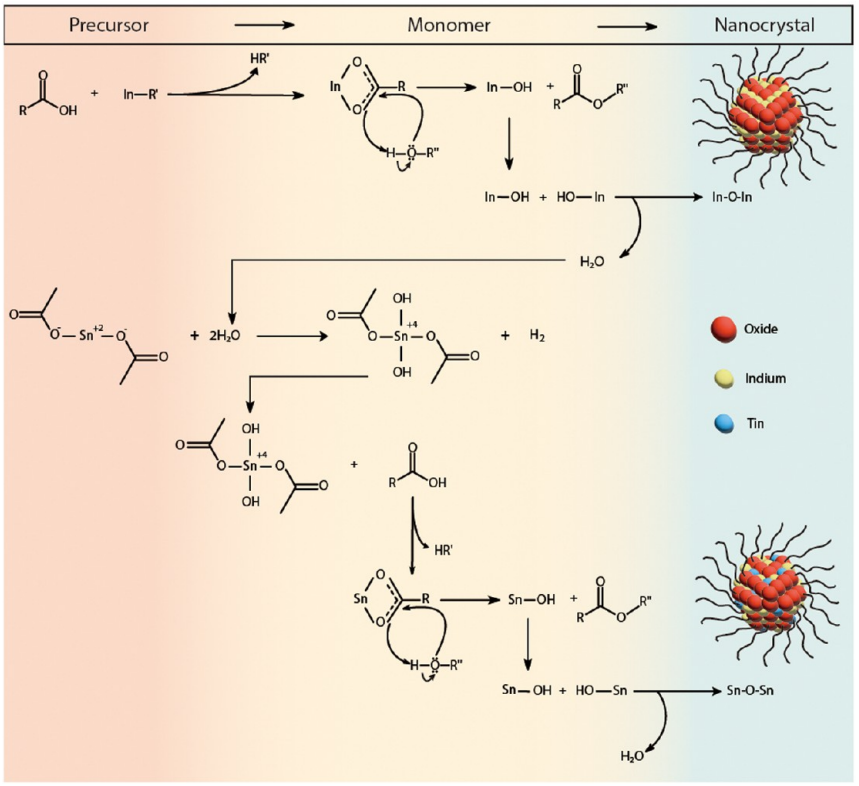

Figure 1. Continuous injection colloidal NC synthesis alcoholysis and hydrolysis mechanism of Sn/In_2O_3 NCs classified into precursor, monomer, and NC growth stages. Sn(II) as the dopant precursor conserved and oxidized into an aliovalent substitutional n-type dopant Sn(IV) valency.

solution color change to dark blue will be observed due to NC formation and growth.

Scale-Up NC Purification. NC is dispersed in a solvent mixed with hexane solvent and IPA antisolvent at a 1:1 ratio and centrifuged at 3600 rpm for 4 min. After centrifugation, the solution supernatant is removed, and the remaining solid pellet material is again dispersed in the hexane solvent through vortex mixing. The IPA antisolvent is added to precipitate the NC at a hexane to IPA volume 1:1 ratio and centrifugation is carried out as before. The NC purification is done 2 times. After 2 cycles of centrifugation, the NC pellet is dispersed into 400 mL of hexane. The NC dispersed in hexane without the antisolvent is centrifuged at 2000 rpm for 3 min to remove any remaining undispersed aggregates. The supernatant liquid with dispersed NCs is collected as the NC solution sample. All NC solution samples were adjusted to a concentration of 40 mg/mL concentration in hexane for characterization and fabrication.

RESULTS AND DISCUSSION

Colloidal synthesis through continuous injection has emerged as a key strategy for the precise control of nucleation and growth in NC fabrication. This method enables improved monodispersity and controllability of particle size and shape, particularly in semiconductor NCs, such as metal chalcogenides and doped oxides, by separating precursor introduction from the thermal nucleation step. Hutchison and collaborators demonstrated the scalability and reproducibility of a continuous injection approach via a flow-based platform, simplifying synthesis conditions by integrating real-time optimization with microfluidic systems.[36−38] These advances highlight the versatility of this method and its central role in tuning the optical and electronic properties of colloidal materials. In addition to the continuous injection method used in this study, applying the Sn(II) doping strategy to the conventional one-pot synthesis method may offer advantages in terms of process simplification and scalability.[39,40] However, this adaptation could affect the delayed doping mechanism of the Sn(II) precursor NCs, potentially hindering the formation of the core−shell structure. The applicability of this approach will be an important subject for future studies focused on large-scale production.[37,38]

In the precursor stage, the reaction between oleic acid and indium acetate occurs as an initial step (Figure 1). Indium acetate undergoes coordination during this step, where the acetate is exchanged with oleic acid and the indium metal becomes coordinated with the carboxyl (−COOH) group. Consequently, an indium−oleate complex (In−OA) is formed in which indium is coordinated with oxygen atoms from oleic acid. In the subsequent monomer stage, the In−OA complex undergoes alcoholysis with an oleyl alcohol. During this reaction, the bond between indium and oxygen is cleaved by oleyl alcohol, resulting in the release of an indium hydroxide (In−OH) intermediate. The formed indium hydroxide undergoes a condensation reaction, releasing water (H_2O) and leading to the formation of an indium oxide (In_2O_3) host NC lattice.[6]

After the In−OH condensation reaction, the H_2O byproduct released during In_2O_3 condensation affects the oxidation state of Sn(II) acetate, which is an n-type dopant precursor, to promote oxidation to the Sn(IV) oxidation valency while generating a hydrogen (H_2) byproduct.[10] The generated Sn(IV) complex reacts with oleic acid present in the precursor stage. Oleic acid and Sn(IV) form a coordination bond and react with oleyl alcohol in the monomer stage. Currently, oleyl alcohol undergoes alcoholysis to generate Sn−OH, and the Sn−OH dopant monomer undergoes a condensation reaction to release H_2O as a byproduct and generate the necessary Sn to

https://doi.org/10.1021/acsami.5c13073
ACS Appl. Mater. Interfaces XXXX, XXX, XXX−XXX

be aliovalent substitutionally doped into the In_2O_3 NC host lattice.[41] Sn(IV) is incorporated as an n-type dopant of Sn/In_2O_3 by substituting indium for the indium oxide lattice structure. As a result, free carriers are generated in the NC lattice, satisfying the Kroger−Vink equation notation for free electron procreation, where × is neutral, • is positive, and ′ is negatively charged defect species.[9,40]

$$(2Sn_{In}\cdot O_i)^{\times} \rightarrow 2Sn_{In}^{\bullet} + \frac{1}{2}O_{2(g)} + 2e' \quad (1)$$

TEM analysis reveals that Sn/In_2O_3 NCs synthesized with Sn(II) and Sn(IV) dopants exhibit a uniform spherical morphology (Figure 2a). The average diameter of Sn/In_2O_3 NCs synthesized using Sn(II) acetate as the dopant precursor was determined to be 18.2 ± 2.3 nm, whereas those synthesized with Sn(IV) acetate exhibited a similar diameter size at 18.3 ± 2.0 nm. These findings indicate that despite the difference in oxidation states of the dopant precursors, the resultant NCs exhibit similar growth characteristics, suggesting that the oxidation state of the tin dopant has a minimal impact on the overall particle size under the given synthetic conditions throughout the growth stage.

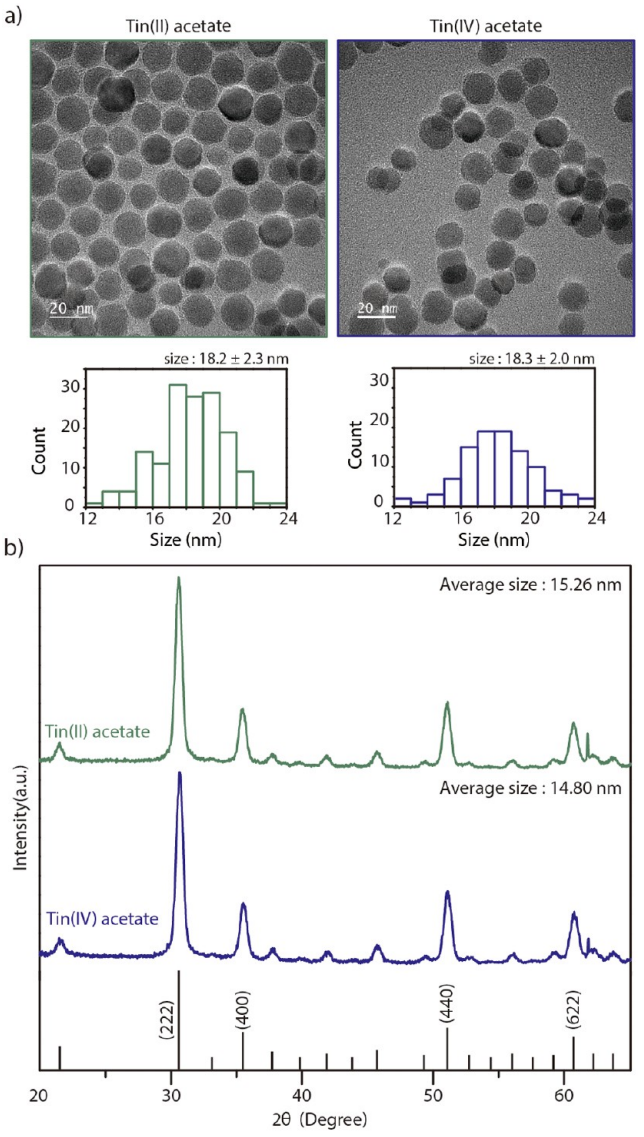

Figure 2. (a) Sn(II) acetate (left) and Sn(IV) acetate (right) dopant precursor NC TEM image (top) and NC diameter size histograms (bottom). Sn(II) dopant precursor NC size was determined to be 18.2 ± 2.3 nm, whereas NCs synthesized with Sn(IV) exhibited a similar diameter size at 18.3 ± 2.0 nm. (b) XRD patterns of Sn(II) and Sn(IV) dopant Sn/In_2O_3 NCs indicate identical In_2O_3 bixbyite phase crystallinity, with dominant (222), (400), (440), and (622) peaks.

X-ray diffraction (XRD) patterns of Sn/In_2O_3 NCs synthesized with comparison dopant oxidation states exhibit well-defined crystallinity. As shown in Figure 2b, both XRD patterns display strong reflections at (222), (400), (440), and (622), which correspond to the bixbyite phase crystal structure of In_2O_3.[9] These results indicate that despite the variation in the oxidation states of the starting precursor dopant, the bixbyite phase of the In_2O_3 crystal lattice remains largely unaffected.[42] This indicates the structural robustness of the host crystal lattice and n-type substitutional aliovalent Sn(IV) oxidation state valency conservation after NC growth. The Scherrer equation, expressed as the following expression, is used to estimate the global crystallite size.[27]

$$D_{hkl} = \frac{K\lambda}{\beta_{hkl}\cos(\theta_{hkl})} \quad (2)$$

Here, K is a dimensionless shape factor, which is generally close to 1. The shape factor is usually assumed to be about 0.9, but it can vary depending on the actual shape of the grains. Therefore, in the text, K is assumed to be 1 for calculations. λ is the X-ray wavelength, β is the fwhm of the intensity peak, and θ is the X-ray incident angle.[43] Using the above equation, the Sn(IV) NC diameter size was 15.3 nm and that of Sn(II) NC was 14.8 nm, suggesting that Sn(II) was synthesized similarly to Sn(IV) when used as a dopant (Figure 2b).[29]

Sn/In_2O_3 NCs synthesized with Sn(IV) and Sn(II) as dopants were dispersed in hexane and visually imaged (Figure 3a) using both visible and SWIR range camera. Through the visible range, both samples appeared transparent with a blue tint, indicating minimal optical absorption in the visible spectrum and a blue tint arising from red-tail absorption from LSPR in the infrared. However, both samples exhibited a pronounced opaque appearance in the SWIR camera images, indicating a strong extinction in the infrared spectral region. Prior studies well indicate Sn/In_2O_3 NCs doped with Sn(IV) exhibit LSPR, enabling high extinction cross sections of SWIR light.[1,44,45] The observation of Sn/In_2O_3 NCs synthesized with Sn(II) as the dopant also displays similar SWIR absorption behavior, which implies that infrared LSPR is observably realized in these NCs. These visual observations suggest that despite the difference in the oxidation state of the tin dopant, the plasmonic characteristics of Sn/In_2O_3 NCs remain preserved, highlighting the potential of Sn/In_2O_3 NCs doped with Sn(II) precursors as an alternative plasmonic material with comparable infrared absorption properties to its Sn(IV) doped counterpart.

FTIR spectroscopy (Figure 3b) was employed to investigate the LSPR characteristics of the Sn/In_2O_3 NC doped with different Sn(IV) and Sn(II) oxidation states of tin precursors. The analysis revealed that the LSPR peak wavenumber for the Sn(IV) acetate-doped Sn/In_2O_3 NCs was 4825.99 cm^{-1}, while that for the Sn(II) acetate-doped Sn/In_2O_3 NCs was 4853.95 cm^{-1}. These results demonstrate that despite the difference in oxidation states of the dopant, the LSPR resonance positions

https://doi.org/10.1021/acsami.5c13073
ACS Appl. Mater. Interfaces XXXX, XXX, XXX−XXX

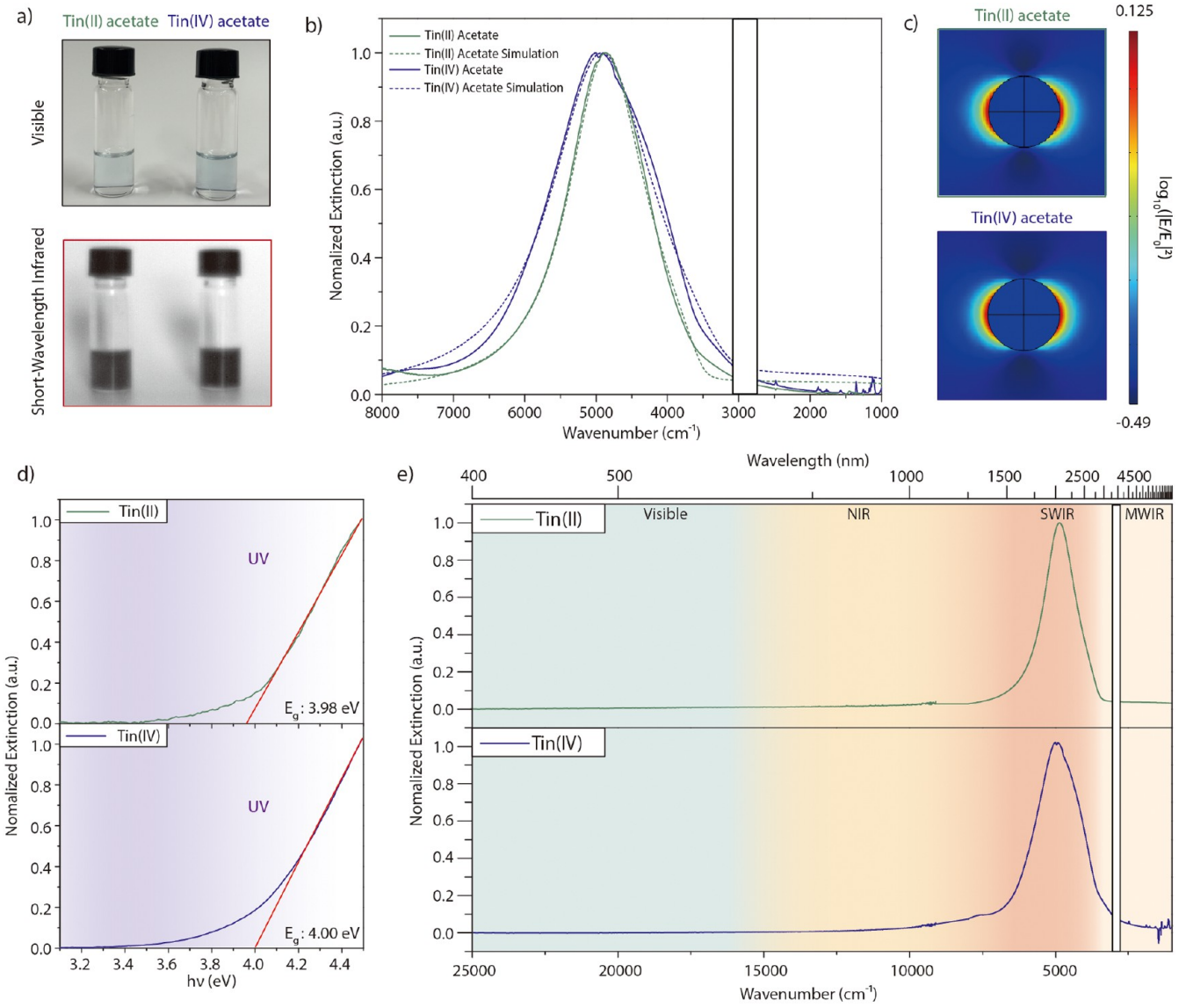

Figure 3. (a) Visible and SWIR camera images of Sn(IV) and Sn(II) dopant precursor Sn/In_2O_3 NCs dispersed in hexane. (b) FTIR spectra of Sn/In_2O_3 NCs synthesized with Sn(IV) and Sn(II) dopant precursors. FTIR measurements are shown as a solid line, while Drude model fitting is represented by the dashed line. (c) Single-particle FEM near-field simulation of Sn(II) and Sn(IV) dopant NCs. (d) Sn(II), Sn(IV) dopant NC band edge Tauc plot with corresponding optical band gap near 4.00 eV. (e) Extended spectral range spectra of Sn(II) and Sn(IV) dopant precursor NCs demonstrating high transparency in the visible (blue region) and strong absorption in the SWIR infrared (red region).

remain remarkably similar. This observation suggests that both Sn(II) and Sn(IV) doping effectively induce free carriers within the Sn/In_2O_3 NCs.[44] Therefore, in addition to the conventional Sn(IV)-based doping strategy, Sn(II) doping presents a viable alternative strategy for achieving comparable plasmonic performance in n-type aliovalent substitutionally doped NCs.

$$\varepsilon_p = \varepsilon_\infty - \frac{\omega_p^2}{\omega^2 + i\omega\gamma} \tag{3}$$

The Drude model is employed to extract the free electron carrier concentration confined within the NC. The optical extinction properties of plasmonic metal oxides are determined by the dielectric function ε_p as a function of frequency (ω). This behavior is described by the Drude model, wherein the collective oscillation of free electron gas is driven by an externally incident electromagnetic field in the infrared range. The position of the extinction peak is influenced by the plasma frequency (ω_P), which depends on the free electron concentration (n_e) localized within the NC. This collective oscillation interaction perturbs the high-frequency dielectric background ε_∞ observed in Sn/In_2O_3. The absorption coefficient (α) is determined by the imaginary loss coefficient (k) component of the dielectric function ε_p, expressed as a function of the frequency (ω). The relationship between absorption and the imaginary loss coefficient is given by $\alpha = \frac{4\pi k}{\lambda}$, where the wavelength λ (cm) can be converted into $\frac{1}{\omega}$ (cm^{-1}) frequency.[2,44]

$$\omega_P = \sqrt{\frac{n_e e^2}{\varepsilon_0 m^*}} \tag{4}$$

The free electron concentration is determined by the relation bulk plasma frequency ω_P and free electron

https://doi.org/10.1021/acsami.5c13073
ACS Appl. Mater. Interfaces XXXX, XXX, XXX−XXX

concentration n_e. Constant e is the elementary electronic charge, ε_0 is the permittivity of free space, and m^* is the electron effective mass. This quantitatively evaluates free electron concentration within the NC domain.[2,44]

$$\gamma(\omega) = \gamma_L - \frac{\gamma_L - \gamma_H}{\pi}\left[\tan^{-1}\left(\frac{\omega - \gamma_X}{\gamma_W}\right) + \frac{\pi}{2}\right] \quad (5)$$

The damping coefficient γ depends on the frequency ω. The damping coefficient applies to an extended Drude model.[2,46,47] γ_L is the low-frequency damping constant, γ_H is the high-frequency constant, γ_X is the crossover frequency, and γ_W is the crossover width.

Sn(IV) and Sn(II) free carrier densities were estimated and compared with the observed LSPR peaks. For each Sn-doped NC, the following carrier concentrations were observed: Sn(IV): 1.04×10^{20} cm^{-3}, Sn(II): 1.05×10^{20} cm^{-3}. For FTIR measurements, the liquid-dispersed NC is observed using a liquid cell with an infrared transparent TCE solvent. Each NC sample in the dielectric medium solution dispersion state is subjected to extended Drude model spectroscopic fitting via MATLAB (Text S1).[46,47] The dielectric medium in which the NCs are dispersed is TCE, which has a dielectric constant of 1.505. The near-field distributions of Sn(IV) acetate and Sn(II) acetate precursor-synthesized NCs simulated through COMSOL finite element method (FEM) simulations with experimentally extracted carrier concentration and damping parameters are shown in Figure 3c.[39,48] The spatial distribution map of the LSPR electromagnetic near-field was simulated at the frequency of the maximum LSPR extinction peak experimentally observed in FTIR spectroscopy (Figure 3b), and the characteristics of the Sn valency dopant precursor NCs were compared. In particular, the magnitudes of the near-field intensity in both Sn(IV) and Sn(II) precursor-doped NCs simulation results are almost similar. Strong electromagnetic field enhancement due to LSPR-induced near-field effect concentrated along the morphological surfaces of NCs was simulated to be at $\log_{10}(|E/E_0|^2)$ magnitude 0.0913 and 0.125 for Sn(IV) and Sn(II), respectively. It was confirmed that Sn(II) has a stronger near-field intensity than Sn(IV). This can be seen in the IR spectrum presented earlier (Figure 3b), where the Sn(II) graph appears sharper than the Sn(IV) graph. This phenomenon occurs because when the attenuation value for LSPR (low-frequency damping (γ_L) at 3553 cm^{-1} for Sn(IV) and 1324 cm^{-1} for Sn(II)) decreases, the near-field intensity increases due to reduced internal scattering, resulting in a narrower and clearer LSPR peak in the IR spectrum. The comparison of the simulation results and the experimental data performed in this study showed a tendency consistent with theoretical analysis, which served as the basis for supporting the reliability of the analysis. This experimental and simulation analysis supports that utilizing differing oxidation states between the Sn(IV) or Sn(II) dopant precursor does not have a significant effect on the near-field and optical properties, suggesting that the Sn(II) valency precursor dopants are oxidized into Sn(IV) during the synthetic mechanism, where dopant valency is conserved toward an LSPR-favorable aliovalent substitutional n-type dopant within the NC host lattice (Table 1).

To analyze the bandgap properties between Sn(IV) or Sn(II) dopant precursor NCs, the optical band gap energy was derived using the Tauc plot analysis (Figure 3d).[49] The Tauc plot shows the relationship between the optical absorption coefficient (α) and the optical energy ($h\nu$) and generally follows the following equation $(ah\nu)^{1/n} = A(h\nu - E_g)$.

Here, α is the optical absorption coefficient, h is the Planck constant, ν is the frequency, A is a material dependent constant, E_g optical bandgap energy, and n is an index determined by the bandgap transition characteristics. The value of n is set to $n = 1/2$ for a direct band gap and $n = 2$ for an indirect band gap. Since ITO is an indirect band gap semiconductor, $n = 2$ was applied for the calculation. The band gap energy was calculated to be 4.00 eV when Sn(IV) was used as a dopant and 3.98 eV for Sn(II).[49,50] Generally, the band gap energy of bulk ITO is reported between 3.5 and 4.3 eV, indicating successful synthesis of Sn/In_2O_3 and supporting the optoelectronic property of Sn/In_2O_3 NCs through the Sn(II) precursor being compatible with the conventional Sn(IV) dopant precursor.[51]

The expanded optical extinction characteristics of Sn/In_2O_3 NCs using Sn(II) and Sn(IV) dopant precursors are shown in the UV−vis−NIR and FTIR integrated spectral data (Figure 3e). Both samples exhibit distinguished LSPR extinction (4000−5000 cm^{-1}, 2000−2500 nm) localized in the SWIR wavelength regions. This is related to the Sn/In_2O_3 NC confined free electron concentration at an $\sim 10^{20}$ cm^{-3} range, being much lower than conventional metals at the $\sim 10^{22}$ cm^{-3} free carrier concentration range.[52] When comparing Sn(II) and Sn(IV) dopant-synthesized NCs, the LSPR resonance peaks of the two spectra are apparent at near similar wavelengths, suggesting that the two dopants impart similar optical properties regardless of the starting Sn(II) dopant precursor oxidation state. Notably, the Sn(IV) sample shows a slightly less symmetrical peak profile in the long-wavelength region (Figure 3e), which we attribute to enhanced scattering effects arising from a broader particle size and shape distribution. Uniform doping distribution at the NC core further contributes to this effect, inducing electron scattering, consistent with the larger low-frequency damping (γ_L) obtained from Drude fitting. In addition, no significant absorption is observed in the visible regions, indicating favorable LSPR resonance targeted to the SWIR spectral range while maintaining high transparency in the visible.[53]

The surface oxidation state in as-synthesized pristine Sn(IV) and Sn(II) dopant precursor Sn/In_2O_3 NCs was analyzed through X-ray photoelectron spectroscopy (XPS) (Figure 4a). For postsynthetic NC and device robustness testing in extreme aerospace conditions, Sn(IV) and Sn(II) dopant precursor Sn/In_2O_3 NCs were exposed to 5 cycles of Mach 1.7 shockwaves. XPS surface analysis was used to distinguish postsupersonic shock surface oxidation states as comparison to the pristine

Table 1. Drude Model Estimated LSPR Properties

	tin(IV) acetate Sn/In_2O_3 NC	tin(II) acetate Sn/In_2O_3 NC
LSPR peak [cm^{-1}]	4826	4854
free carrier density n_c [cm^{-3}]	1.04×10^{20}	1.05×10^{20}
bulk plasma frequency ω_p [cm^{-1}]	13,998	14,083
low-frequency damping constant γ_L [cm^{-1}]	3553	1324
high-frequency damping constant γ_H [cm^{-1}]	982	883
crossover frequency γ_X [cm^{-1}]	4641	5227
crossover width γ_W [cm^{-1}]	1387	109

https://doi.org/10.1021/acsami.5c13073
ACS Appl. Mater. Interfaces XXXX, XXX, XXX−XXX

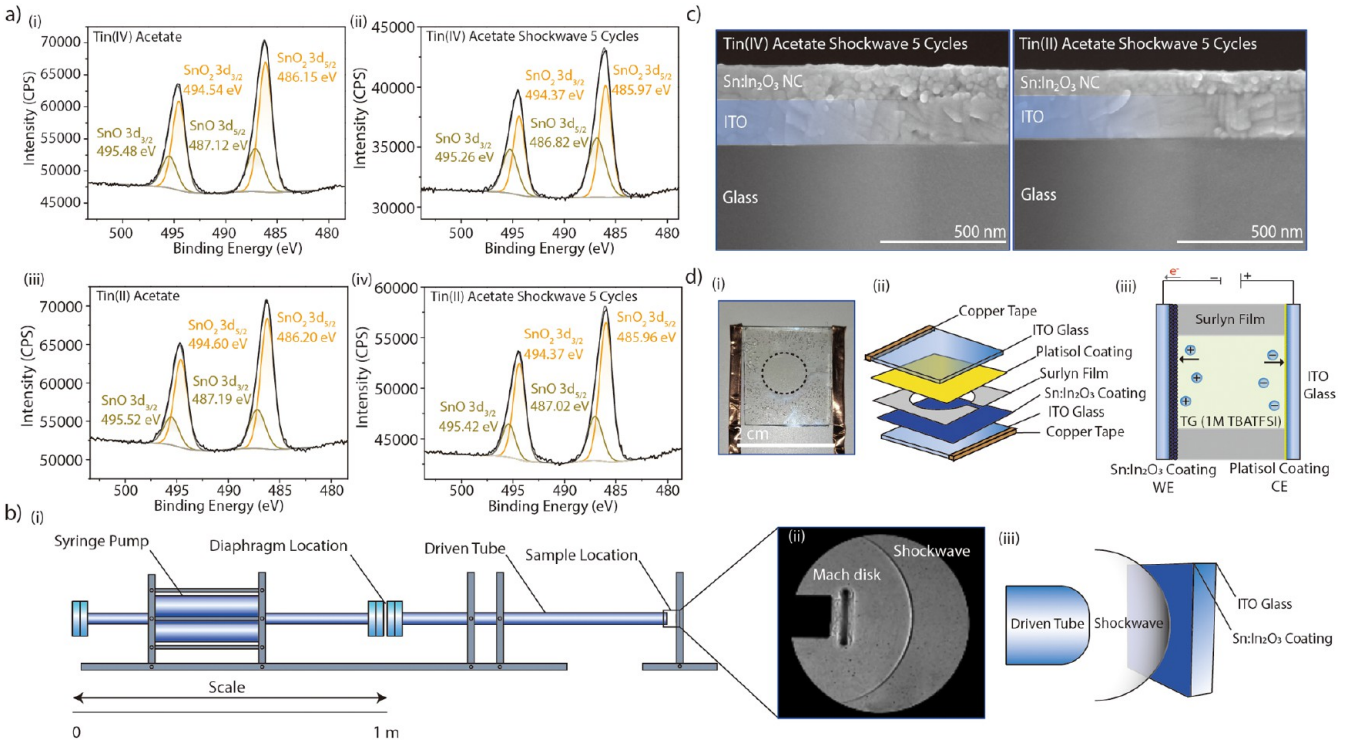

Figure 4. (a) XPS spectra of pristine Sn(IV) precursor-doped Sn/In_2O_3 NC for SnO_2 $3d_{3/2}$ and SnO_2 $3d_{5/2}$ doublet peak, and SnO $3d_{3/2}$ and SnO $3d_{5/2}$ doublet peak (i). The peaks are designated as Sn(IV) oxidation state SnO_2 species (orange) and Sn(II) oxidation state SnO species (tan). Post shockwave exposure (5 cycles, Mach 1.7) for the Sn(IV) precursor-doped NC (ii). Pristine Sn(II) precursor-doped NC (iii) and post shockwave exposure for Sn(II) precursor-doped NC (iv) comparative spectra. (b) Supersonic shock test experimental setting schematic composed of syringe pump, diaphragm, driver, driven tube, and sample location stage (i). Schlieren imaging taken with a high-speed camera show the primary shockwave shadow phase created by the light from the light source and reflected by the reflector. We observed a shockwave in the form of a bow shock (right) and a Mach disk (left) in the form of a remnant column (ii). Shockwave schematic from the driven tube illustrating shock impact on the Sn/In_2O_3 NC coated film facing the sample location stage (iii). (c) Cross-section scanning electron microscopy (SEM) images of the Sn/In_2O_3 NC film on the ITO glass substrate. Sn(IV) precursor-doped Sn/In_2O_3 NC (left) and Sn(II) precursor-doped Sn/In_2O_3 NC thin-film cross-sectional (right) images after 5 cycles of shockwave exposure at Mach 1.7. Scale bars are at 500 nm. (d) Image of the fabricated SOG device. The IR light probe penetrates the circular optical window at the device center. The working electrode (WE) and CE have been extended with copper tape. The scale bar is at 2 cm (i). Device assembly schematic design (ii). A schematic representation of internal cross-sectional architecture of the MLC device (iii).

NC surface. By deconvoluting analyzing the NC sample series, the surface oxidation valency conservation of the dopant is distinguished. Sn(IV) valency SnO_2 $3d_{5/2}$, SnO_2 $3d_{3/2}$, and Sn(II) valency SnO $3d_{5/2}$, SnO $3d_{3/2}$ doublet peak deconvolution produced two types of surface oxidation for reference Sn(IV) and Sn(II) oxidation state species, respectively (Table 2). The surface chemical bond energies of each oxidation species were referenced by using the NIST X-ray Photoelectron Spectroscopy Database.

SnO_2 and SnO doublet $3d_{5/2}$ and $3d_{5/2}$ peaks are observed in the photoelectron emission signal of the Sn(IV) precursor-doped NC, and the same peak species are observed in the Sn(II) precursor-doped NC photoelectron emission signal. Preshock Sn(IV) precursor-doped Sn/In_2O_3 NCs are observed with SnO_2 $3d_{5/2}$ $3d_{3/2}$ doublet peaks (486.15 eV, 494.54 eV) and SnO $3d_{5/2}$, $3d_{3/2}$ doublet peaks (487.12 eV, 495.48 eV). Preshock Sn(II) preshock-doped NCs are observed as SnO_2 $3d_{5/2}$ $3d_{3/2}$ doublet peaks (485.97 eV, 494.37 eV) and SnO $3d_{5/2}$, $3d_{3/2}$ doublet peaks (486.82 eV, 495.26 eV). The results provide evidence for n-type dopant oxidation valency conservation in both types of NC.[S4]

Furthermore, XPS analysis revealed a modest increase in the SnO contribution and a corresponding decrease in the intensity of the SnO_2 signal following shockwave exposure (Table 2). We attribute this to surface-localized effects, likely caused by mechanical spallation during the supersonic impact, which may have exposed subsurface Sn(II) species that were initially embedded within the NCs. Given the surface sensitivity of XPS, such exposure can alter the apparent oxidation state without affecting the bulk electronic structure. Importantly, these changes do not impact the overall LSPR characteristics or the electrochemical device behavior. This complements the evidence for the conversion of Sn(II) dopant to Sn(IV) during the synthesis step and demonstrates the high resistance to shock testing and oxidative stability of both

Table 2. XPS Peak Deconvolution

component [%]	tin(IV)	tin(II)	tin(IV) shockwave	tin(II) shockwave
Sn−O_2	71.06	73.55	58.22	60.0
Sn−O	28.94	26.45	41.78	40.0
		Doublet Sn $3d_{5/2}$		
SnO_2 (486.2 eV)	42.64	44.13	34.93	43.95
SnO (487.0 eV)	17.36	15.87	25.07	29.30
		Doublet Sn $3d_{3/2}$		
SnO_2 (494.5 eV)	28.42	29.42	23.29	16.05
SnO (494.5 eV)	11.58	10.58	16.71	10.70

https://doi.org/10.1021/acsami.5c13073
ACS Appl. Mater. Interfaces XXXX, XXX, XXX−XXX

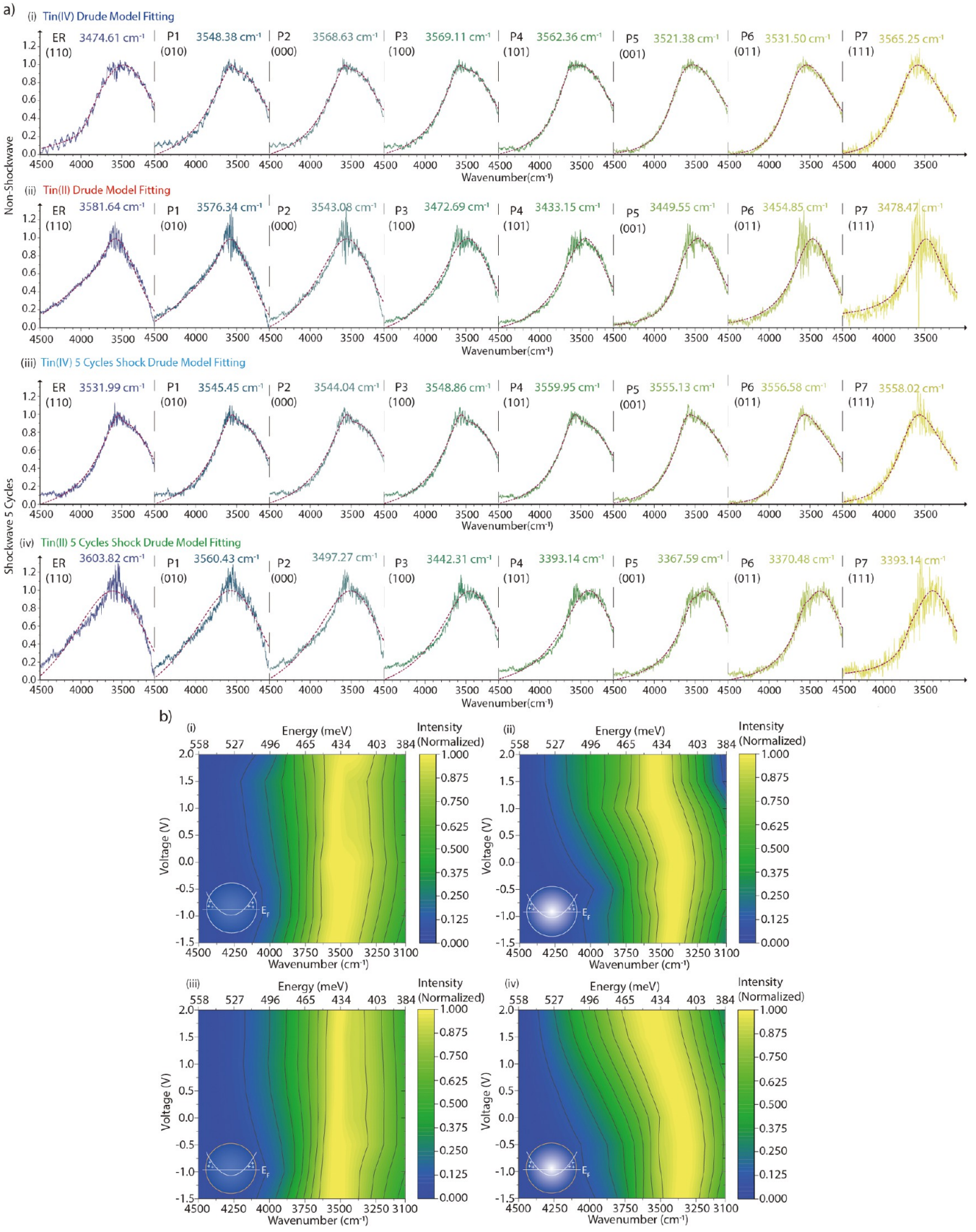

Figure 5. (a) In situ FTIR spectra of Sn/In_2O_3 NC devices with the Drude model fitting curve overlaid on a graph with normalizing values. The wavenumber frequency of each maximum LSPR peak is texted in each respective graph inset. The change of the maximum phase value is expressed as a data read operation in the form of an MLC bit. (b) In situ FTIR spectra of Sn/In_2O_3 NC devices with Drude model Fitting. The data were implemented as a contour heat map, showing the normalized intensity map through energy (meV) and wavenumber (cm^{-1}) as a function of

https://doi.org/10.1021/acsami.5c13073
ACS Appl. Mater. Interfaces XXXX, XXX, XXX−XXX

Figure 5. continued

applied voltage potential (V). The inset NC figures show the energy band Fermi level of the NC and the depletion tuning. In the (i,iii) inset NC, the free electrons are uniformly distributed across the NC. However, in (ii,iv) inset NCs, the free electrons are segmentally distributed on the surface.

valency precursor types of NC. The NC surface reacts to the shockwave test to anticipate oxygen defects. This interferes with the infrared absorption of the NC.[20] Although two spin-coating steps were employed, the resulting NC film sufficiently behaved as a single continuous layer without a discernible interfacial gap. The second spin-coating step wets and penetrates the first layer with interparticle adhesion rather than creating an optically or electronically isolated interface.[55]

The supersonic shock exposure test schematic is shown in Figure 4b(i).[56] The shockwave is driven by pressure and the rupture of a diaphragm plate, generating a compressed shockwave through the driver tube. Schlieren imaging taken with a high-speed camera shows the pressure wave arriving near the end wall of the tube, creating a bow-shaped shockwave and a donut-shaped Mach disk (Figure 4b(ii)).[56,57] The sample was directly exposed to the bow-shaped main shockwave to perform the shock exposure experiment. The Sn/In_2O_3 NC film coated on the ITO glass substrate was directly exposed to the shockwave (Figure 4b(iii)). NC film samples were fixed to the sample stage wall, 2 cm away from the end of the driven tube. After five shockwave cycles, cross-sectional SEM images were taken to confirm the presence and robustness of the NC-coated film (Figure 4c). We observed a homogeneous NC film in both sample cross section images. The Sn(IV) NC film thickness (left) is 118 nm, and the Sn(II) NC film (right) thickness is 74 nm, confirming preservation of the NC film after supersonic shockwave exposure prior to device fabrication.

A fabricated glass substrate MCL device is shown in Figure 4d(i), measuring 2 cm × 2 cm with copper tape extension on both sides for working and CE interconnect. The circle-shaped dotted line in the center is the optical window with a 1 cm diameter for in situ FTIR measurement use in detecting the plasmonic switching state. The device assembly schematic in Figure 4d(ii) shows the device fabrication layer in five layers. The Surlyn film, a thermoformed polymer adhesion layer, was cut to accommodate and stack an electrolyte tight sandwich layer between the Sn/In_2O_3 NC-coated ITO glass substrate and the Platisol-coated ITO glass substrate. Coating the CE substrate with Platisol increases the rate of CE electron transfer, resulting in favorable higher charge density and consequently enhanced capacitance for the Sn/In_2O_3 NC-coated WE.[58] The Surlyn film was then heated to 60 °C and pressed to thermoform the two substrates together. The device was injected with the TMATFSI liquid electrolyte inside through capillary wetting action for applying a gating electrical field. A cross-sectional view schematic of the assembled device is shown in Figure 4d(iii).

When a positive voltage potential is applied, the migration of ions inside the electrolyte transports cations (TMA^+) to the WE and anions to the CE.[34] LSPR spectra for the applied voltages from the electrochemical device were collected through in situ FTIR measurements. A total of four devices were fabricated, with a Sn(IV) precursor-doped NC device (Figure S2(i)), a Sn(II) precursor-doped NC device (Figure S2(ii)), a Sn(IV) precursor-doped NC and shockwave-exposed device (Figure S2(iii)), and a Sn(II) precursor-doped NC and shockwave-exposed device (Figure S2(iv)). The LSPR peak extinction intensity was highest at (2 V) and lowest at (−1.5 V). The LSPR peak modulation was examined by Drude model fitting through MATLAB to characterize the surface depletion effect induced by red-shifting of the LSPR peak. The most oxidized electron-depleted state is 2 V and the most reduced electron-rich state is −1.5 V for all the voltage-modulated devices. The direct observation of shifting LSPR peak position values demonstrates that the plasmonic device is analogous to driving a unique memory state in a flash memory device.

The data read operation of a three-bit memory triple level MLC can be distinguished and expressed as a function of a surface-depleted NCs' red-shifted LSPR peak position (Figure 5a(i−iv)).[34,59] This is noted in the upper left corner of the individual state spectral plot. We visually represented the intensity and modulation of the LSPR peaks in Figure 5b(i−iv), where the yellow color indicates regions of high LSPR peak extinction intensity and the blue color indicates low extinction baseline intensity. This graph was plotted through the Drude model fitting data peak fit extracted from Figure 5a. The behavior of the LSPR peak's red-shifted frequency modulation as a function of applied voltage potential is plotted as a line graph in Figure S2. In the Sn(II) precursor dopant NC fabricated device (red) and postshock-exposed device (green), operation of the LSPR modulation state data as an MLC state is observed in the voltage to the LSPR peak position function plot.

For Sn(IV) precursor dopant NC devices, such observation of LSPR red-shifted MLC state modulation is interestingly not prominent compared to the Sn(II) precursor dopant NC MLC states. In previous studies, the surface depletion-induced red-shift modulation of the LSPR peak varied depending on the concentration of the dopant procreated free carriers localized in the NC. This is attributed to the NC surface depletion width induced by the incoming positive charge cation TMA^+ onto the NC surface. The surface depletion width effectively penetrates easily toward the NC core for doped semiconductor NCs with lower free carrier concentrations as compared to higher free carrier concentration NCs.[4,60] It is previously observed by Zandi et al. that surface depletion-induced LSPR peak red-shifting is minimal for NCs synthesized with dopant concentration at and above Sn 5% at.[34,53] This is a similar observation to the Sn(IV) precursor dopant NCs with identical Sn(IV) dopant Sn 5% at. dopant concentration Sn/In_2O_3 NC synthetic conditions.

In the Sn(II) precursor dopant NCs, favorable LSPR red-shifting state modulation is observed as compared to that in Sn(IV) precursor dopant NCs, despite similar free carrier concentrations confined within the NC domain in both synthetic specimens. This enhanced surface depletion effect can be attributed to n-type active $Sn_{In}^{\bullet}$ aliovalent substitutional dopants being delayed and incorporated radially toward the NC surface during particle growth.[3] It can be attributed mechanistically that the n-type inactive Sn(II) dopants are incompletely converted to Sn(IV) valency during the initial stages of growth. This is due to incomplete In−OH hydrolysis

https://doi.org/10.1021/acsami.5c13073
ACS Appl. Mater. Interfaces XXXX, XXX, XXX−XXX

condensation water byproduct formation during In_2O_3 NC host lattice growth when the NC particle size is small. Through gradual accumulation of a water byproduct during NC size growth, the Sn(II) dopant is favorably converted to an n-type active Sn(IV) dopant. This results in a chemically induced radial distribution of higher free electron active $Sn_{In}^{\bullet}$ dopant site concentration toward the NC surface during synthesis growth.[53,54] With radial distribution of n-type active dopants and free carriers to the Sn(II) precursor dopant NC surface, surface depletion is favorable as cation charge-induced depletion length more effectively penetrates the free electron-rich NC surface, contributing to the observed LSPR red-shift modulable MLC device states.[2,61]

While the degree of surface-segregated dopant distribution can be observed by the in situ FTIR spectra, it would be difficult to photophysically characterize the plasmonic properties of unique single particles at a single NC level. Therefore, we directly observed the infrared LSPR signature of the plasmonic near field generated by a single NC. Characterization was performed by MAC-STEM-EELS (monochromated aberration-corrected, scanning transmission electron microscopy-electron energy loss spectroscopy).

Mapping the near-field localization of LSPR modes in STEM is possible by sub-Angstrom diameter electron beam probes after direct electron microscopy sampling.[62] EELS with the recently developed monochromation technique allows observation at mid-infrared frequencies. A spatial map is created from the spectral image, and the area of interest is precisely scanned with the beam to measure the spectrum pixel by pixel. This creates a three-dimensional spatial data set, consisting of two spatial dimensions and one spectral dimension, generating a spatially resolved LSPR EELS map. We deconvolve the individual plasmon modes using the Non-Negative Matrix Factorization (NMF) method.[63] Thus, we deconvolve all localized spatial (away, surface, particle) and spectral (bulk, surface) components and use the NMF technique, which provides accurate and sharp resolution of plasmon modes in STEM-EELS signal data.[48,63,64]

The images and near-field maps acquired by STEM-EELS observed each single particle of Sn(IV) precursor dopant NC (a) and Sn(II) precursor dopant NC (b) postexposed to 5 cycles of supersonic shockwave at Mach 1.7. The single particle observation locations were classified into away (light blue), surface (blue), and particle (dark blue) to identify all localized spatial components (Figure 6a,b(i)). And the near-field imaging data were divided spectrally into bulk mode and surface mode for direct imaging observation (Figure 6a,b-a,b(ii,iii)). The peak energy loss spectrum of each NC was marked on the top of the image. The deconvolution graph of LSPR near-field mode of each NC was composed of away (light blue line), surface (blue line), particle (bark blue line), bulk mode (red area), and surface mode (cyan area) (Figure 6a,b(iv)). The particle (dark blue line) in bulk mode (red area) is strongly observed in the Sn(IV) precursor dopant NC. On the other hand, in the Sn(II) precursor dopant NC, the particle (dark blue line) in bulk mode (red area) is observed weakly and the surface (blue line) in surface mode (sky area) is observed strongly. The rationale for the higher observed intensity difference at the Sn(II) NC surface mode is due to the segregated core−shell dopant distribution and favorable Fermi level above the conduction band minimum that were observed through in situ FTIR spectral experiments, shown in Figure 5b.[41] This is caused by the difference in the free

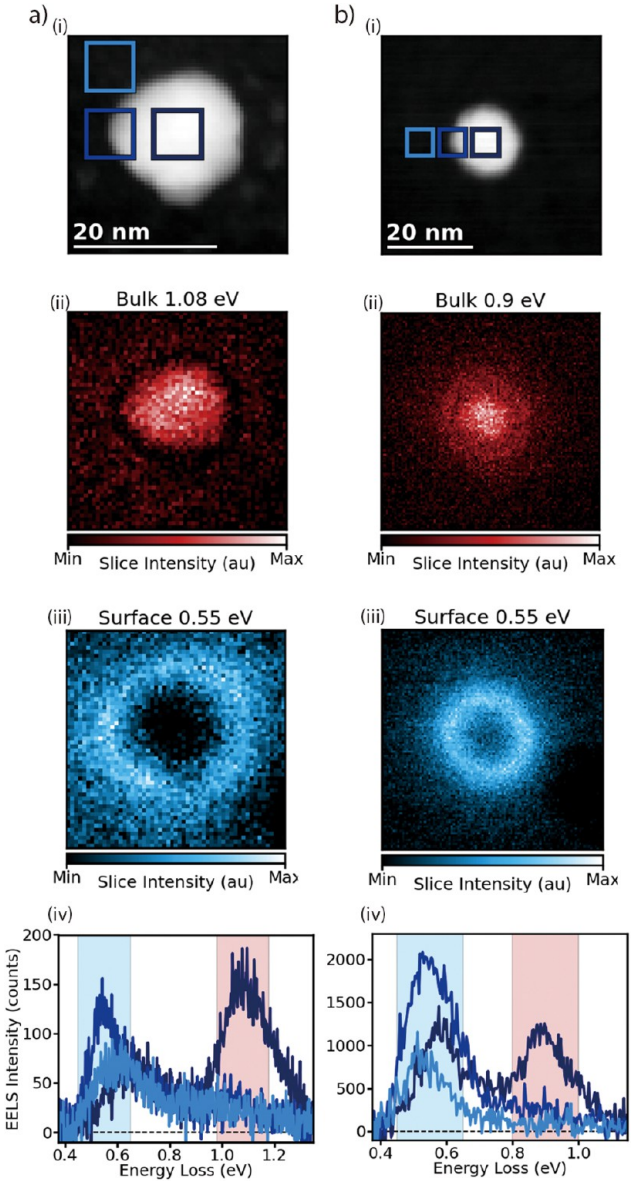

Figure 6. Single-particle STEM-EELS near-field maps of Sn(IV)-doped Sn/In_2O_3 NC (a) and Sn(II)-doped Sn/In_2O_3 NC (b) exposed to 5 cycles of shockwave. Single-particle observation localized at away (light blue), surface (blue), and particle (dark blue) (i). STEM-EELS image maps displayed in NC bulk mode (ii) and NC surface mode (iii). The peak area of each NC is shown at the top of the image. An NMF deconvoluted STEM-EELS spectrum shown as away (sky line), surface (blue line), particle (dark blue line), bulk mode (red area), and surface mode (cyan area) (iv).

electron carrier distribution between the two Sn(II) and Sn(IV) dopant precursor valency NCs. Therefore, the doping is delayed during the synthesis of Sn(II) precursor dopant NC as compared to Sn(IV), which causes the formation of free electrons to be radiantly concentrated on the NC surface.[41,54] STEM-EELS near-field image maps observed in the trimer aggregated state NC particles (Figures S8 and S9) suggest that even NCs with supersonic shock exposure under ensemble configuration retain and behave with plasmonic near-field LSPR effects.

To investigate the effect of the oxidation state of doping precursors on carrier distribution, we combined STEM−EELS mapping and COMSOL simulation.[34] Near-field decomposi-

https://doi.org/10.1021/acsami.5c13073
ACS Appl. Mater. Interfaces XXXX, XXX, XXX−XXX

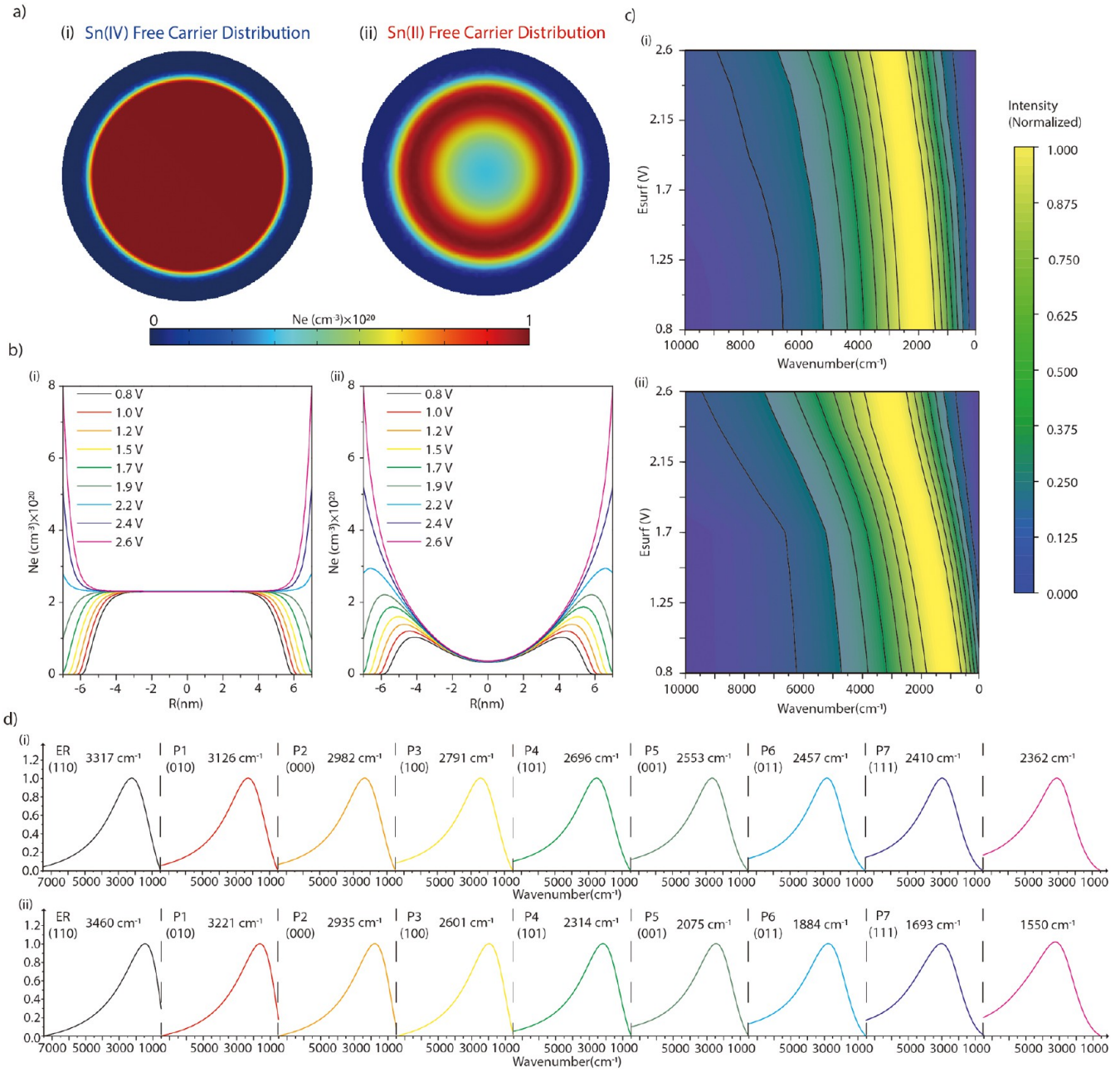

Figure 7. (a) Using COMSOL FEM, we calculated n_e (carrier concentration) as a function of radius from Poisson's equation. We show the NC model with a cross-sectional map of n_e. Sn(IV) precursor dopant NC model (a(i)) and Sn(II) precursor dopant NC model (a(ii)) are shown at stable intrinsic states of 0.8 V. (b) Steps of E_{surf} (surface electric field) profiles for n_e as a function of NC model radius. The Sn(IV) precursor dopant NC model (b(i)) exhibits a uniform n_e distribution at the NC core. The Sn(II) precursor dopant NC model (b(ii)) exhibits an gradated n_e distribution with a lower n_e concentration toward the center of the radius. (c) Normalized optical LSPR contour heat map that calculates the LSPR intensity of spherical nanoparticles using the Maxwell−Garnett theory for the Sn(IV) precursor dopant NC model (c(i)) and Sn(II) precursor dopant NC model (c(ii)) n_e profiles. (d) Normalized LSPR peak graph of the Sn(IV) precursor dopant NC model (d(i)) and the Sn(II) precursor dopant NC model (d(ii)), simulated using the Maxwell−Garnett equation. The maximum peak wavenumber frequency of each LSPR is indicated in text within the graph.

tion analysis (Figure 6a,b(iv)) revealed that Sn(IV)-doped NCs exhibited strong bulk mode (particle) contributions, whereas Sn(II)-doped NCs showed enhanced surface mode intensity. This difference is attributed to the separated core−shell doping distribution of Sn(II) NCs, and the in situ FTIR results (Figure 5b) support this, showing a higher Fermi level above the conduction band minimum.

To quantitatively analyze the carrier distribution, the Poisson equation for a spherical NC model was solved using the stepwise surface electric field (E_{surf}) function and the FEM in COMSOL (Supporting Information Figure S6). The Sn(IV) NC model (Figure 7a(i)) exhibited a uniform carrier distribution throughout the core, while the Sn(II) NC model (Figure 7a(ii)) showed a radial gradient due to the delay in the conversion of Sn(II) to n-type active Sn(IV) during the growth process. Stepwise E_{surf} profiles (carrier concentration n_e versus radius, Figure 7b(i,ii)) confirmed that the surface −OH groups of the ligand passivate oxide defects, reducing n_e near the

https://doi.org/10.1021/acsami.5c13073
ACS Appl. Mater. Interfaces XXXX, XXX, XXX−XXX

surface in both models.[65] In Sn(II) NCs, this depletion phenomenon extends deeper toward the core, increasing the depletion length and thereby enhancing overall carrier control.[53]

The n_e profiles obtained from COMSOL were used in Maxwell−Garnett theory calculations in MATLAB, including iterative effective permittivity evaluations (Supporting Information Text S5). The resulting normalized optical LSPR contour maps (Figure 7c(i,ii)) and peak positions (Figure 7d(i,ii)) demonstrated that Sn(II)-doped NCs achieve greater LSPR red shift control than did Sn(IV)-doped NCs. This enhanced control is consistent with experimental FTIR and optical control results (Figures 5b and S9), which are attributed to the combined effects of radial carrier distribution, delayed activation of dopants within the core, and preferential introduction of dopants near the surface, thereby enhancing the surface depletion effect without damaging the NC structure.[53,54]

To demonstrate the scale-up industrial scalability of alternative Sn(II) dopant valency precursor synthesized NCs, Figure 8 shows the FTIR spectra of Sn/In_2O_3 NC obtained

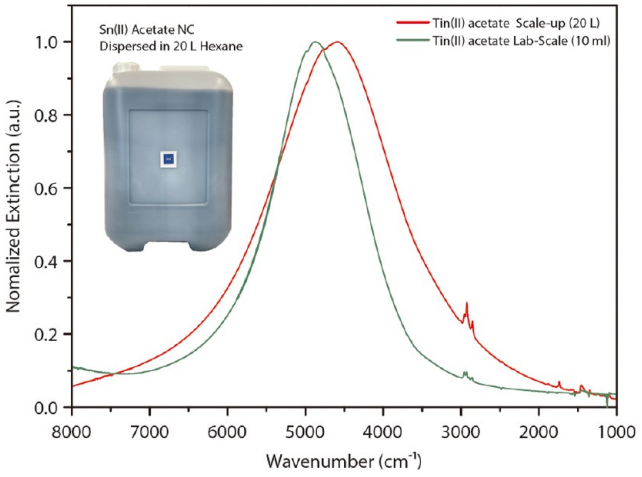

Figure 8. FTIR spectra of Sn/In_2O_3 NC synthesized with identical Sn(II) acetate dopant, with scaled-up Sn/In_2O_3 NCs (red) and lab-scale Sn/In_2O_3 NCs (green). Sn(II) acetate dopant precursor synthesized 20 L batch Sn/In_2O_3 NCs dispersed in hexane.

under the synthetic conditions scaled up to a 20 L batch volume NC solution product, compared to Sn/In_2O_3 NCs obtained under prior lab scale synthesis. Both spectra show similar LSPR peaks at 4700 cm^{-1}, with the scaled-up Sn/In_2O_3 NC at 4593 cm^{-1} and the lab-scaled Sn/In_2O_3 NC at 4867 cm^{-1}. This demonstrates that the plasmonic LSPR properties are maintained under larger batch reaction conditions for Sn(II) dopant precursor NCs at a level similar to that of lab-scale NCs used in the study.[66,67] In particular, the concurrence of LSPR peaks in the scaled-up sample means that the electron concentration is stably maintained, demonstrating that consistent doping control and synthetic reproducibility through Sn(II) precursor doping were secured under industrial scale reactions.[1,25] Figure 8 shows a photograph of the scaled-up Sn/In_2O_3 NC synthesized product, redispersed in 20 L of hexane at 20 mg/mL NC solution. It can be visually confirmed that the dispersed NC solution has a characteristic blue tint color. This color is due to the infrared LSPR extinction red-tail absorption edge characteristics, and synthesized NCs were successfully dispersed in nonpolar hexane solution with the desired SWIR range optical properties maintained. These scalability results suggest that the commercial-scale expansion of Sn/In_2O_3 NCs doped with Sn(II) valency precursors is feasible in the near future.[7,40]

CONCLUSION

The doped n-type Sn/In_2O_3 NC synthesized by the continuous injection colloidal method demonstrates infrared range LSPR, induced by confining free electron carriers in the NC space. Sn/In_2O_3 NCs are conventionally synthesized using an identical oxidation valency Sn(IV) precursor to the n-type aliovalent substitutional dopant Sn^{4+} within the In^{3+} host site; we observed that the same density of free electron carriers at 1.05×10^{20} cm^{-3} could be generated using the Sn(II) dopant precursor. We proposed a mechanism in which H_2O generated by the reaction of indium acetate with oleic acid in the precursor step induces the oxidation of Sn(II) to generate Sn(IV). The size, shape, and crystalline characteristics of the NC were compared by TEM and XRD analyses. The infrared LSPR absorption peaks were also observed to be near identical. To test the robustness of the NCs, the surface oxidation state was characterized by XPS after exposure to Mach 1.7 shockwave five times, and the surface oxidation was shown to be retained when comparing before and after shock exposure. The deposition of the NC on the glass substrate was observed by SEM cross section imaging analysis.

An optical MLC memory device is fabricated by integrating plasmonic NCs onto a glass substrate. We observed surface depletion-induced LSPR peak shift through in situ infrared spectra detection with the fabricated device, and it was possible to realize MCL-type memory devices. The device with Sn(II) dopant precursor NCs had an enhanced LSPR peak shift attributed to delayed dopant precursor oxidation and NC incorporation from Sn(II) to Sn(IV) during NC growth. The activated n-type Sn(IV) oxidation valency dopant is radially segregated to the NC surface, where a surface depletion effect occurs effectively as compared to Sn(IV) dopant precursor-synthesized NCs.[54] We have directly observed the plasmonic LSPR near-field of microscopic single particles. The characterization was confirmed by image maps using MAC-STEM-EELS.[62] After deconvolution of all spatial and spectral components, particle LSPR in bulk mode is strongly observed in the conventional Sn(IV) precursor-doped NC.[48,64] On the other hand, Sn(II) precursor-doped NCs are strongly observed at the surface position, providing direct observation of dopant surface segregation due to the delayed doping incorporation of Sn(II) precursor dopant during NC continuous growth.[54]

In this study, we confirmed the feasibility of replacing the conventional Sn(IV) substrate with Sn(II) and demonstrated the feasibility of economical mass production and mass production by using a cost-effective Sn(II) acetate dopant precursor. We also demonstrated the robustness of plasmonic NCs for aerospace and high-speed flight environment-compatible technologies. NCs with durability to extreme shockwave environments have potential for application in aerospace technologies such as SWIR range LIDAR, infrared heat tracking sensor technology, and spectral band-filter for infrared range sunlight glare shielding.[17,22] With the increasing importance of glass substrate technology, we also confirmed the robustness of NCs on glass substrates and fabricated devices to demonstrate the operation of MCL state modulable memory devices. This study aims to provide an economical

https://doi.org/10.1021/acsami.5c13073
ACS Appl. Mater. Interfaces XXXX, XXX, XXX−XXX

and efficient synthesis strategy for Sn/In_2O_3 NCs that can enable further integration of next-generation semiconductor and optoelectronic devices exploiting LSPR properties in the near future.[32,68,69]

■ ASSOCIATED CONTENT

Supporting Information

The Supporting Information is available free of charge at https://pubs.acs.org/doi/10.1021/acsami.5c13073.

Details in COMSOL FEM near-field simulation, Drude model fitting MATLAB code NC free carrier concentration estimation, MATLAB simulation of Maxwell–Garnett effective medium LSPR absorption spectrum, and Maxwell–Garnett equation based LSPR peak maxima shift MATLAB simulation (PDF)

■ AUTHOR INFORMATION

Corresponding Authors

Ikhyun Kim − *Department of Mechanical Engineering, Keimyung University, Daegu 42601, Republic of Korea;* orcid.org/0000-0002-5916-9244; Email: kimih@kmu.ac.kr

Shin Hum Cho − *Department of Chemical Engineering, Keimyung University, Daegu 42601, Republic of Korea;* orcid.org/0000-0002-0271-116X; Email: shinhum@kmu.kr

Authors

Do Yoon Park − *Department of Chemical Engineering, Keimyung University, Daegu 42601, Republic of Korea*

Ju Hyeon Kang − *Department of Chemical Engineering, Keimyung University, Daegu 42601, Republic of Korea*

Sivaprakash Paramasivam − *Department of Mechanical Engineering, Keimyung University, Daegu 42601, Republic of Korea*

Gordon Duddy − *Department of Chemistry and Biochemistry, University of Notre Dame, Notre Dame, Indiana 46556, United States*

Jordan A. Hachtel − *Center for Nanophase Materials Sciences, Oak Ridge National Laboratory, Oak Ridge, Tennessee 37831, United States;* orcid.org/0000-0002-9728-0920

Jon P. Camden − *Department of Chemistry and Biochemistry, University of Notre Dame, Notre Dame, Indiana 46556, United States;* orcid.org/0000-0002-6179-2692

Complete contact information is available at: https://pubs.acs.org/10.1021/acsami.5c13073

Notes

The authors declare no competing financial interest.

■ ACKNOWLEDGMENTS

This work was supported by the 2024 Bisa Research Grant of Keimyung University (20220648) and supported by the RISE (Regional Innovation System & Education) at Keimyung University. This work was also supported by the National Research Foundation of Korea (NRF) grant funded by the Korea government (MSIT) (RS-2025-00557769). XPS was performed using the K-ALPHA + system at the Korea Basic Science Institute (KBSI), Busan Center (Jong-Seong Bae). SEM analysis was supported by the Daegu Technopark Nano Convergence Commercialization Center (Miyeon Bae). Supersonic impact environments for NC device components were provided by Keimyung University (I.K. and Shivaprakash Paramasivam). TEM analysis was carried out at the Institute of Next-Generation Semiconductor Convergence Technology, DGIST (Minyoung Lee). Monochromated STEM-EELS analysis was supported by the Center for Nanophase Materials Sciences (CNMS), a U.S. Department of Energy Office of Science User Facility, using instrumentation within the Materials Characterization Core at Oak Ridge National Laboratory, provided by UT-Battelle, LLC, under Contract No. DE-AC05-00OR22725.

■ REFERENCES

(1) Agrawal, A.; Cho, S. H.; Zandi, O.; Ghosh, S.; Johns, R. W.; Milliron, D. J. Localized Surface Plasmon Resonance in Semiconductor Nanocrystals. *Chem. Rev.* **2018**, *118* (6), 3121−3207.

(2) Mendelsberg, R. J.; Garcia, G.; Li, H.; Manna, L.; Milliron, D. J. Understanding the Plasmon Resonance in Ensembles of Degenerately Doped Semiconductor Nanocrystals. *J. Phys. Chem. C* **2012**, *116* (22), 12226−12231.

(3) Jansons, A. W.; Hutchison, J. E. Continuous Growth of Metal Oxide Nanocrystals: Enhanced Control of Nanocrystal Size and Radial Dopant Distribution. *ACS Nano* **2016**, *10* (7), 6942−6951.

(4) Agrawal, A.; Johns, R. W.; Milliron, D. J. Control of Localized Surface Plasmon Resonances in Metal Oxide Nanocrystals. *Annu. Rev. Mater. Res.* **2017**, *47*, 1−31.

(5) Blemker, M. A.; Gibbs, S. L.; Raulerson, E. K.; Milliron, D. J.; Roberts, S. T. Modulation of the Visible Absorption and Reflection Profiles of ITO Nanocrystal Thin Films by Plasmon Excitation. *ACS Photonics* **2020**, *7* (5), 1188−1196.

(6) Donaldson, J. D.; Moser, W.; Simpson, W. B. 1147. Tin(II) Acetates. *J. Chem. Soc. Resumed* **1964**, No. 0, 5942−5947.

(7) Sawyer, A. K.; Frey, C. A Simple Synthesis of Tin(IV) Acetate from Tetraphenyltin. *Synth. React. Inorg. Met.-Org. Chem.* **1983**, *13* (2), 259−262.

(8) Schmidt, H.; Blohm, C.; Jander, G. Solvolysereaktionen in Essigsäureanhydrid Die Darstellung von Germanium- Und Zinntetraacetat. *Angew. Chem., Int. Ed.* **1947**, *59* (7−8), 233−237.

(9) Cho, S. H.; Roccapriore, K. M.; Dass, C. K.; Ghosh, S.; Choi, J.; Noh, J.; Reimnitz, L. C.; Heo, S.; Kim, K.; Xie, K.; Korgel, B. A.; Li, X.; Hendrickson, J. R.; Hachtel, J. A.; Milliron, D. J. Spectrally Tunable Infrared Plasmonic F,Sn:In2O3 Nanocrystal Cubes. *J. Chem. Phys.* **2020**, *152* (1), 014709.

(10) Pascual, J.; Nasti, G.; Aldamasy, M. H.; Smith, J. A.; Flatken, M.; Phung, N.; Di Girolamo, D.; Turren-Cruz, S.-H.; Li, M.; Dallmann, A.; Avolio, R.; Abate, A. Origin of Sn(II) Oxidation in Tin Halide Perovskites. *Mater. Adv.* **2020**, *1* (5), 1066−1070.

(11) Raza, I.; Mehmood, N. HYPERSONIC WEAPON SYSTEMS − A NEW WAVE OF ARMS RACE IN THE INDIAN OCEAN REGION. *Margalla Pap.* **2023**, *27* (1), 28−39.

(12) Alkire, B.; Nacouzi, G.; Aguirre, J.; Dolan, B. *A Missile Jamming and Engagement Model*; RAND Corporation, 2025. https://www.rand.org/pubs/research_reports/RRA3150-2.html (accessed March 25, 2025).

(13) Bates, C.; Lucas, J.; Robinson, J. The Javelin Integrated Flight Simulation. In *Computational Science-ICCS 2001*; Alexandrov, V. N., Dongarra, J. J., Juliano, B. A., Renner, R. S., Tan, C. J. K., Eds.; Springer: Berlin, Heidelberg, 2001; pp 507−514.

(14) Reeves, C.; Weinbaum, C. *China, Russia, and the United States in Low Earth Orbit: Space Assets, Counterspace Capabilities, and Launch Systems*; RAND Corporation, 2025. https://www.rand.org/pubs/tools/TLA3139-1.html (accessed March 25, 2025).

(15) Cho, S. H.; Kim, I. Hypersonic Shockwave Robustness in Infrared Plasmonic Doped Metal Oxide Nanocrystal Cubes: Implications for High-Speed Ballistics Transport Applications. *ACS Appl. Nano Mater.* **2022**, *5* (12), 17487−17495.

(16) Gao, X.; Hu, M.; Fu, Y.; Weng, L.; Liu, W.; Sun, J. Response of MoS2-Sb2O3 Film to Low-Earth-Orbit Space Environment. *Mater. Lett.* **2018**, *227*, 161−164.

(17) Roriz, R.; Cabral, J.; Gomes, T. Automotive LiDAR Technology: A Survey. *IEEE Trans. Intell. Transp. Syst.* **2022**, *23* (7), 6282−6297.
(18) Kim, I.; Martins, R. J.; Jang, J.; Badloe, T.; Khadir, S.; Jung, H.-Y.; Kim, H.; Kim, J.; Genevet, P.; Rho, J. Nanophotonics for Light Detection and Ranging Technology. *Nat. Nanotechnol.* **2021**, *16* (5), 508−524.
(19) Franke, D.; Harris, D. K.; Chen, O.; Bruns, O. T.; Carr, J. A.; Wilson, M. W. B.; Bawendi, M. G. Continuous Injection Synthesis of Indium Arsenide Quantum Dots Emissive in the Short-Wavelength Infrared. *Nat. Commun.* **2016**, *7* (1), 12749.
(20) Underwood, G. W. Transparencies for Supersonic and Hypersonic Flight. *Aircr. Eng. Aerosp. Technol.* **1964**, *36* (12), 379−408.
(21) Dreyer, L. Latest Developments on SpaceX's Falcon 1 and Falcon 9 Launch Vehicles and Dragon Spacecraft. In *2009 IEEE Aerospace Conference*, 2009; pp 1−15.
(22) Kalaiarasi, S.; Sivakumar, A.; Martin Britto Dhas, S. A.; Jose, M. Shock Wave Induced Anatase to Rutile TiO2 Phase Transition Using Pressure Driven Shock Tube. *Mater. Lett.* **2018**, *219*, 72−75.
(23) Sivakumar, A.; Soundarya, S.; Jude Dhas, S. S.; Bharathi, K. K.; Dhas, S. A. M. B. Shock Wave Driven Solid State Phase Transformation of Co3O4 to CoO Nanoparticles. *J. Phys. Chem. C* **2020**, *124* (19), 10755−10763.
(24) Schimpf, A. M.; Lounis, S. D.; Runnerstrom, E. L.; Milliron, D. J.; Gamelin, D. R. Redox Chemistries and Plasmon Energies of Photodoped In2O3 and Sn-Doped In2O3 (ITO) Nanocrystals. *J. Am. Chem. Soc.* **2015**, *137* (1), 518−524.
(25) Hamberg, I.; Granqvist, C. G.; Berggren, K.-F.; Sernelius, B. E.; Engström, L. Band-Gap Widening in Heavily Sn-Doped In2O3. *Phys. Rev. B:Condens. Matter Mater. Phys.* **1984**, *30* (6), 3240−3249.
(26) Liu, Y.; Mustain, W. E. Stability Limitations for Pt/Sn−In2O3 and Pt/In−SnO2 in Acidic Electrochemical Systems. *Electrochim. Acta* **2014**, *115*, 116−125.
(27) Wescott, E. M.; Sentman, D. D.; Heavner, M. J.; Hallinan, T. J.; Hampton, D. L.; Osborne, D. L. The Optical Spectrum of Aircraft St. Elmo's Fire. *Geophys. Res. Lett.* **1996**, *23* (25), 3687−3690.
(28) Mayandi, J.; Finstad, T. G.; Venkatesan, R.; Ponniah, V.; Karazhanov, S.; Venkatachalapathy, V. Carbon-Dioxide as Annealing Atmosphere to Retain the Electrical Properties of Indium-Tin Oxide. *Mater. Lett.* **2020**, *276*, 128195.
(29) Intel. Intel Provides Update on Internal Foundry Model, Newsroom. https://newsroom.intel.com/corporate/intel-provides-update-on-internal-foundry-model (accessed April 1, 2025).
(30) Intel Unveils Industry-Leading Glass Substrates to Meet Demand for More Powerful Compute, Intel Corporation. https://www.intc.com/news-events/press-releases/detail/1647/intel-unveils-industry-leading-glass-substrates-to-meet (accessed March 26, 2025).
(31) Kotasthane, P.; Manchi, A. *When the Chips are Down: A Deep Dive into a Global Crisis*; Bloomsbury Publishing, 2023.
(32) Rathore, J. S.; Fandan, R.; Srivastava, S.; Khiangte, K. R.; Das, S.; Ganguly, U.; Laha, A.; Mahapatra, S. Self-Assembled Sn Nanocrystals as the Floating Gate of Nonvolatile Flash Memory. *ACS Appl. Electron. Mater.* **2019**, *1* (9), 1852−1858.
(33) Buisman, K.; Nanver, L. K.; Scholtes, T. L. M.; Schellevis, H.; de Vreede, L. C. N. High-Performance Varactor Diodes Integrated in a Silicon-on-Glass Technology. In *Proceedings of 35th European Solid-State Device Research Conference*, ESSDERC 2005, 2005; pp 117−120.
(34) Zandi, O.; Agrawal, A.; Shearer, A. B.; Reimnitz, L. C.; Dahlman, C. J.; Staller, C. M.; Milliron, D. J. Impacts of Surface Depletion on the Plasmonic Properties of Doped Semiconductor Nanocrystals. *Nat. Mater.* **2018**, *17* (8), 710−717.
(35) Lee, H. W.; Papadakis, G.; Burgos, S. P.; Chander, K.; Kriesch, A.; Pala, R.; Peschel, U.; Atwater, H. A. Nanoscale Conducting Oxide PlasMOStor. *Nano Lett.* **2014**, *14* (11), 6463−6468.
(36) Epps, R. W.; Felton, K. C.; Coley, C. W.; Abolhasani, M. Automated Microfluidic Platform for Systematic Studies of Colloidal Perovskite Nanocrystals: Towards Continuous Nano-Manufacturing. *Lab Chip* **2017**, *17* (23), 4040−4047.
(37) Abdel-Latif, K.; Epps, R. W.; Bateni, F.; Han, S.; Reyes, K. G.; Abolhasani, M. Self-Driven Multistep Quantum Dot Synthesis Enabled by Autonomous Robotic Experimentation in Flow. *Adv. Intell. Syst.* **2021**, *3* (2), 2000245.
(38) de Mello Donegá, C.; Liljeroth, P.; Vanmaekelbergh, D. Physicochemical Evaluation of the Hot-Injection Method, a Synthesis Route for Monodisperse Nanocrystals. *Small* **2005**, *1* (12), 1152−1162.
(39) Choi, S.-I.; Nam, K. M.; Park, B. K.; Seo, W. S.; Park, J. T. Preparation and Optical Properties of Colloidal, Monodisperse, and Highly Crystalline ITO Nanoparticles. *Chem. Mater.* **2008**, *20* (8), 2609−2611.
(40) Kanehara, M.; Koike, H.; Yoshinaga, T.; Teranishi, T. Indium Tin Oxide Nanoparticles with Compositionally Tunable Surface Plasmon Resonance Frequencies in the Near-IR Region. *J. Am. Chem. Soc.* **2009**, *131* (49), 17736−17737.
(41) Gassenbauer, Y.; Schafranek, R.; Klein, A.; Zafeiratos, S.; Hävecker, M.; Knop-Gericke, A.; Schlögl, R. Surface States, Surface Potentials, and Segregation at Surfaces of Tin-Doped In2O3. *Phys. Rev. B:Condens. Matter Mater. Phys.* **2006**, *73* (24), 245312.
(42) Cho, S. H.; Ghosh, S.; Berkson, Z. J.; Hachtel, J. A.; Shi, J.; Zhao, X.; Reimnitz, L. C.; Dahlman, C. J.; Ho, Y.; Yang, A.; Liu, Y.; Idrobo, J.-C.; Chmelka, B. F.; Milliron, D. J. Syntheses of Colloidal F:In2O3 Cubes: Fluorine-Induced Faceting and Infrared Plasmonic Response. *Chem. Mater.* **2019**, *31* (7), 2661−2676.
(43) Patterson, A. L. The Scherrer Formula for X-Ray Particle Size Determination. *Phys. Rev.* **1939**, *56* (10), 978−982.
(44) Lounis, S. D.; Runnerstrom, E. L.; Llordés, A.; Milliron, D. J. Defect Chemistry and Plasmon Physics of Colloidal Metal Oxide Nanocrystals. *J. Phys. Chem. Lett.* **2014**, *5* (9), 1564−1574.
(45) Mergel, D.; Qiao, Z. Dielectric Modelling of Optical Spectra of Thin In2O3: Sn Films. *J. Phys. Appl. Phys.* **2002**, *35* (8), 794.
(46) Mendelsberg, R. J.; Garcia, G.; Milliron, D. J. Extracting Reliable Electronic Properties from Transmission Spectra of Indium Tin Oxide Thin Films and Nanocrystal Films by Careful Application of the Drude Theory. *J. Appl. Phys.* **2012**, *111* (6), 063515.
(47) Runnerstrom, E. L.; Bergerud, A.; Agrawal, A.; Johns, R. W.; Dahlman, C. J.; Singh, A.; Selbach, S. M.; Milliron, D. J. Defect Engineering in Plasmonic Metal Oxide Nanocrystals. *Nano Lett.* **2016**, *16* (5), 3390−3398.
(48) Nicoletti, O.; de la Peña, F.; Leary, R. K.; Holland, D. J.; Ducati, C.; Midgley, P. A. Three-Dimensional Imaging of Localized Surface Plasmon Resonances of Metal Nanoparticles. *Nature* **2013**, *502* (7469), 80−84.
(49) Tauc, J. Optical Properties and Electronic Structure of Amorphous Ge and Si. *Mater. Res. Bull.* **1968**, *3* (1), 37−46.
(50) Feigenbaum, E.; Diest, K.; Atwater, H. A. Unity-Order Index Change in Transparent Conducting Oxides at Visible Frequencies. *Nano Lett.* **2010**, *10* (6), 2111−2116.
(51) Khan, A.; Rahman, F.; Nongjai, R.; Asokan, K. Structural Optical and Electrical Transport Properties of Sn Doped In2O3. *Solid State Sci.* **2020**, *109*, 106436.
(52) Quinn, J. J.; Yi, K.-S. Free Electron Theory of Metals. In *Solid State Physics: Principles and Modern Applications*; Quinn, J. J., Yi, K.-S., Eds.; Springer International Publishing: Cham, 2018; pp 83−112.
(53) Ghini, M.; Curreli, N.; Lodi, M. B.; Petrini, N.; Wang, M.; Prato, M.; Fanti, A.; Manna, L.; Kriegel, I. Control of Electronic Band Profiles through Depletion Layer Engineering in Core−Shell Nanocrystals. *Nat. Commun.* **2022**, *13* (1), 537.
(54) Lounis, S. D.; Runnerstrom, E. L.; Bergerud, A.; Nordlund, D.; Milliron, D. J. Influence of Dopant Distribution on the Plasmonic Properties of Indium Tin Oxide Nanocrystals. *J. Am. Chem. Soc.* **2014**, *136* (19), 7110−7116.
(55) Garcia, G.; Buonsanti, R.; Runnerstrom, E. L.; Mendelsberg, R. J.; Llordes, A.; Anders, A.; Richardson, T. J.; Milliron, D. J. Dynamically Modulating the Surface Plasmon Resonance of Doped Semiconductor Nanocrystals. *Nano Lett.* **2011**, *11* (10), 4415−4420.

https://doi.org/10.1021/acsami.5c13073
ACS Appl. Mater. Interfaces XXXX, XXX, XXX−XXX

(56) Kim, I.; Shim, H.; Kim, Y.; Park, G. Effect of Shock-Heated Flow on Morphological and Structural Properties of Anatase TiO2 Nanoparticles. *Mater. Lett.* **2021**, *294*, 129793.
(57) Sakthivel, S.; Paramasivam, S.; Velusamy, P.; Jerries Infanta, J. A. D.; Ragavendran, V.; Mayandi, J.; Arumugam, S.; Kim, I. Experimental Investigation of Structural, Morphological, and Optical Characteristics of SrTiO3 Nanoparticles Using a Shock Tube for Photocatalytic Applications. *Z. Phys. Chem.* **2024**, *238* (10), 1863−1885.
(58) Furukawa, S.; Iino, H.; Iwamoto, T.; Kukita, K.; Yamauchi, S. Characteristics of Dye-Sensitized Solar Cells Using Natural Dye. *Thin Solid Films* **2009**, *518* (2), 526−529.
(59) Melikyan, A.; Lindenmann, N.; Walheim, S.; Leufke, P. M.; Ulrich, S.; Ye, J.; Vincze, P.; Hahn, H.; Schimmel, T.; Koos, C.; Freude, W.; Leuthold, J. Surface Plasmon Polariton Absorption Modulator. *Opt. Express* **2011**, *19* (9), 8855−8869.
(60) Dahlman, C. J.; Heo, S.; Zhang, Y.; Reimnitz, L. C.; He, D.; Tang, M.; Milliron, D. J. Dynamics of Lithium Insertion in Electrochromic Titanium Dioxide Nanocrystal Ensembles. *J. Am. Chem. Soc.* **2021**, *143* (22), 8278−8294.
(61) Caldwell, M. A.; Raoux, S.; Wang, R. Y.; Philip Wong, H. S.; Milliron, D. J. Synthesis and Size-Dependent Crystallization of Colloidal Germanium Telluride Nanoparticles. *J. Mater. Chem.* **2010**, *20* (7), 1285−1291.
(62) García de Abajo, F. J. Optical Excitations in Electron Microscopy. *Rev. Mod. Phys.* **2010**, *82* (1), 209−275.
(63) Roccapriore, K. M.; Ziatdinov, M.; Cho, S. H.; Hachtel, J. A.; Kalinin, S. V. Predictability of Localized Plasmonic Responses in Nanoparticle Assemblies. *Small* **2021**, *17* (21), 2100181.
(64) Hachtel, J. A.; Lupini, A. R.; Idrobo, J. C. Exploring the Capabilities of Monochromated Electron Energy Loss Spectroscopy in the Infrared Regime. *Sci. Rep.* **2018**, *8* (1), 5637.
(65) Kriegel, I.; Urso, C.; Viola, D.; De Trizio, L.; Scotognella, F.; Cerullo, G.; Manna, L. Ultrafast Photodoping and Plasmon Dynamics in Fluorine−Indium Codoped Cadmium Oxide Nanocrystals for All-Optical Signal Manipulation at Optical Communication Wavelengths. *J. Phys. Chem. Lett.* **2016**, *7* (19), 3873−3881.
(66) Park, D.-Y.; Cho, S.-H. Metallic Degenerately Doped Free-Electron-Confined Plasmonic Nanocrystal and Infrared Extinction Response. *Metals* **2024**, *14* (8), 843.
(67) Pu, Y.; Cai, F.; Wang, D.; Wang, J.-X.; Chen, J.-F. Colloidal Synthesis of Semiconductor Quantum Dots toward Large-Scale Production: A Review. *Ind. Eng. Chem. Res.* **2018**, *57* (6), 1790−1802.
(68) Dionne, J. A.; Diest, K.; Sweatlock, L. A.; Atwater, H. A. PlasMOStor: A Metal−Oxide−Si Field Effect Plasmonic Modulator. *Nano Lett.* **2009**, *9* (2), 897−902.
(69) Lüth, H. Tunneling in Semiconductor Nanostructures: Physics and Devices. *Acta Phys. Pol. A* **1996**, *90* (4), 667−679.

https://doi.org/10.1021/acsami.5c13073
ACS Appl. Mater. Interfaces XXXX, XXX, XXX−XXX